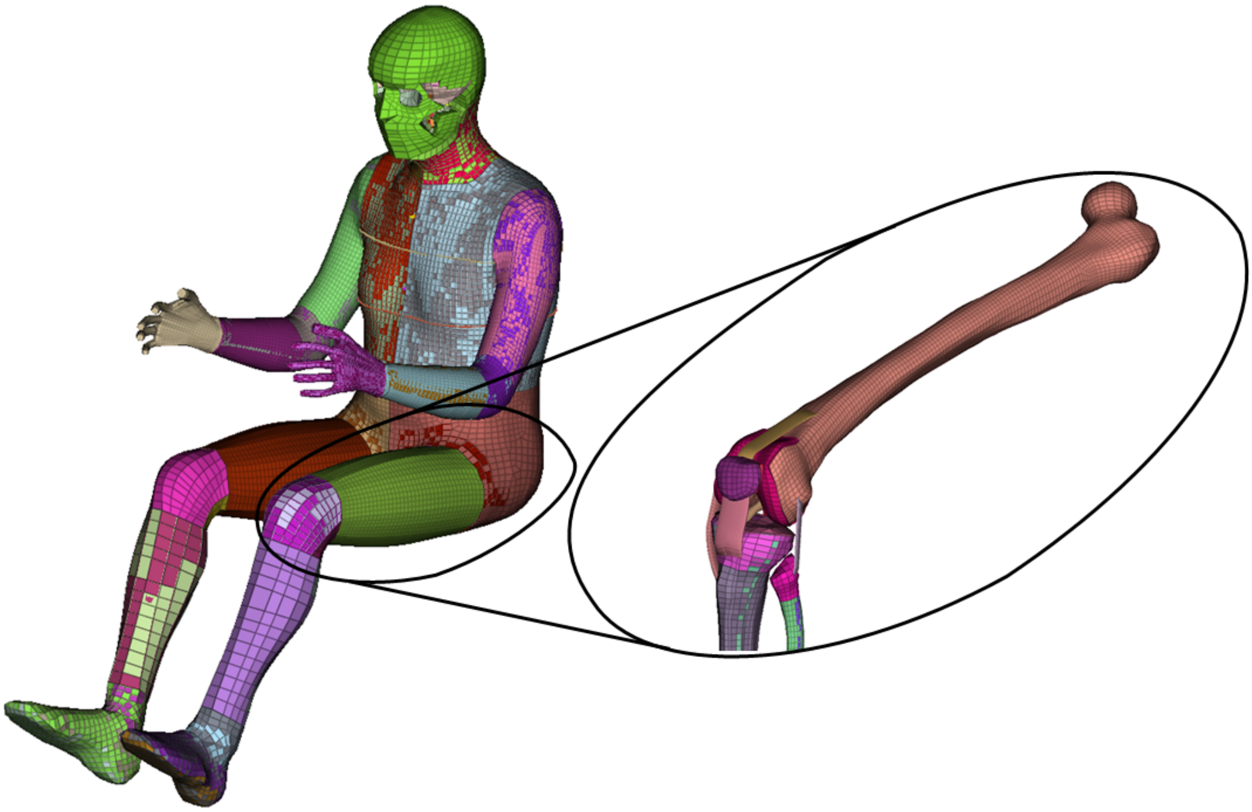

Finite Element Modelling of Knee Joint and Femur for Future Injury Assessment

Master's thesis in Applied Mechanics

GUSTAV SVENSSON

DEPARTMENT OF MECHANICS AND MARITIME SCIENCES

CHALMERS UNIVERSITY OF TECHNOLOGY
Gothenburg, Sweden 2022
www.chalmers.se

Master's thesis 2022

Finite Element Modelling of Knee Joint and Femur for Future Injury Assessment

GUSTAV SVENSSON

CHALMERS
UNIVERSITY OF TECHNOLOGY

Department of Mechanics and Maritime Sciences
Division of Vehicle Safety
Chalmers University of Technology
Gothenburg, Sweden 2022

Finite Element Modelling of Knee Joint and Femur for Future Injury Assessment
GUSTAV SVENSSON

Supervisor: Johan Iraeus, Department of Mechanics and Maritime Sciences
Bengt Pipkorn, Autoliv Inc.

Examiner: Johan Iraeus, Department of Mechanics and Maritime Sciences

Master's Thesis 2022:73
Department of Mechanics and Maritime Sciences
Division of Vehicle Safety
Chalmers University of Technology
SE-412 96 Gothenburg
Telephone +46 31 772 1000

Cover: Seated 50^{th} percentile male SAFER HBM v10 and modelled knee joint and femur.

Typeset in LaTeX
Printed by Chalmers Reproservice
Gothenburg, Sweden 2022

Finite Element Modelling of Knee Joint and Femur for Future Injury Assessment
GUSTAV SVENSSON
Department of Mechanics and Maritime Sciences
Chalmers University of Technology

Abstract

The purpose of this thesis was to develop and validate a FE model of the femur and knee with associated ligaments, tendons and cartilage. In the future, the model will be integrated into the SAFER HBM representing a 50^{th} percentile male and used to develop the capability of the SAFER HBM to assess femur and knee injury risk.

In total, eleven parts, including the femur, patella, anterior cruciate ligament, posterior cruciate ligament, medial collateral ligament, lateral collateral ligament, patellar tendon, quadriceps tendon and cartilage on the distal end of the femur, posterior side of the patella and on the tibial plateau, were modelled using eight node solid elements. The femur and the patella models are based on geometry models from a CT scan of a 50^{th} percentile female, and the soft tissue models are based on geometry descriptions found in the literature. The cortical and trabecular bone tissues of the femur and the patella were modelled with isotropic material properties. All models were meshed in accordance to the requirements and quality criteria of SAFER HBM standards.

The femur was validated against previously published three-point-bending and combined loading tests. 23 tests were replicated using explicit LS-DYNA simulations. Two methods were used to evaluate the correlation between the tests and the simulations. The response of the simulations, reaction force of the actuator versus actuator displacement, were plotted together with statistically evaluated corridors, ± 2 standard deviations of the mean reaction, from the tests. To assess the correlation in an objective sense, a CORA evaluation was made on the time-history results. The results showed that the average time-force CORA score were 0.720 and 0.752 for the three-point-bending set and the combined load set. This CORA score corresponds to good biofidelity.

Keywords: Finite Element Modelling, Validation, Knee, Femur, Human Body Model, SAFER.

Preface and acknowledgements

This thesis is the final project of my studies at the master's programme in Applied Mechanics at Chalmers University of Technology. It was carried out during the spring of 2022 at the division of Vehicle Safety, department of Mechanics and Maritime sciences.

Firstly, I would like to thank my supervisors Johan Iraeus and Bengt Pipkorn for given me the opportunity to work with this thesis and exploring a fraction of the complex field of biomechanics.

Secondly, I would like to thank Jobin John, John Ek, Linus Lundin and the others at the division of Vehicle Safety for discussions, professional guidance and support throughout the thesis.

Thirdly, I would like to thank Magnus Ekh and the rest of the professors, teacher assistants and administrative staff involved at the master's programme in Applied Mechanics for knowledge and support during the two last years.

Lastly, I would like to thank my family. For all support and love over the years, and the years to come.

Gustav Svensson, Gothenburg, June 2022

List of Acronyms

Below is the list of acronyms that have been used throughout this thesis, listed in alphabetical order:

ACL	Anterior Cruciate Ligament
AIS	Abbreviated Injury Scale
AP	Anterior-Posterior
ATD	Anthropomorphic Test Device
BLB	Bone-Ligament-Bone
CORA	CORrelation and Analysis
CT	Computed Tompgraphy
FE	Finite Element
FEM	Finite Element Method
GHBMC	Global Human Body Models Consortium
HBM	Human Body Model
KTH	Knee-Thigh-Hip
LCL	Lateral Colateral Ligament
LM	Lateral-Medial
MCL	Medial Collateral Ligament
ML	Medial-Lateral
PA	Posterior-Anterior
PEL	Potted External length
PCL	Posterior Cruciate Ligament
PMHS	Post Mortem Human Subject
PMMA	PolyMethyl MethAcrylate
PT	Patellar Tendon
QT	Quadriceps Tendon
SD	Standard Deviation
THUMS	Total Human model for Safety

Contents

List of Figures

List of Tables

1 Introduction

Each year, road traffic accidents claims 1.35 million lives and up to 50 million non-fatal injuries occurs worldwide [1]. One of the most vulnerable road user groups are the pedestrians, and it represents 23% of all fatalities worldwide [1]. In frontal impacts of vehicles, the most frequently injured body part of an occupant restraint by belt and airbag is the lower extremities [2]. The most frequent injured body parts in a pedestrian accident are the lower extremities [3]–[6]. Injuries to the lower extremities will not often cause fatalities but can lead to long term impairment which is costly for the society and a tragedy to the individuals.

The most widely used scale of classification of injuries is the Abbreviated Injury Scale (AIS), which ranges from AIS0, non-injured, to AIS6, currently untreatable, [2]. The knee is one of the most frequently injured body parts, and injuries to the knee are classified as moderate to medium severity (AIS2) [6], [7]. Knee fractures as patella fracture and femoral condyle fracture, soft-tissue injuries as ligament lacerations and ruptures are examples of knee injuries classified as AIS2. 45% of all AIS2 injuries of the knee are soft-tissue injuries [7]. If considering AIS3+, the combined severity levels above and including AIS3, injuries to the femur are more frequent.

It is important to mitigate the risk of injuries to the lower extremities, especially to the knee and femur. A first step to mitigate severe injuries is to understand why they occur and thereafter develop mitigation strategies, such as restraint systems or safety systems.

Historically, different approaches have been used by researchers in vehicle safety to study and analyse the response of a human in vehicle impacts. They have used volunteer tests, cadaver tests or Post-Mortem-Human-Subjects (PMHS) tests, crash tests using Anthropomorphic Test Devices (ATD) and more recently simulating impacts using mathematical models, Human Body Models (HBM).

By use of the Finite Element Method (FEM), a region can be discretized into smaller elements to solve differential equations, which describes the physical problem and holds over the regions [8]. This method can be applied to models of humans to offer a detailed analysis and to evaluate the response, on tissue level, of the human body exposed to external loading [2]. State-of-the-art Finite Element (FE) HBMs are used within the automotive industry to analyse different crash scenarios and to develop restraint systems to mitigate the risk of severe injuries, and in the worst scenario causing fatalities. There are several developers and versions of HBMs, e.g.

Total HUman Model for Safety (THUMS) [9], [10], Global Human Body Models Consortium (GHBMC) [11], [12], VIVA+, SAFER HBM, etc. The SAFER HBM is a refinement of THUMS v3.

For an HBM to be useful and trustworthy, it must be validated to assure biofidelity. The recommended usage of an HBM is restricted by the validation of the HBM. E.g., if an HBM will be used to assess pedestrian injuries to the thigh, it must be validated against a load cases which resembles the load case of a pedestrian impact.

The lower extremities of the THUMS 6.1 and GHBMC 5.1 have been validated for kinetics and kinematics through three-point-bending, femoral head impact and impacts of the Knee-Thigh-Hip (KTH) complex. Three-point-bending of the shaft tests and femoral head impact test was used as validation for the 50^{th} percentile female femur of VIVA+ [13].

Previous focus for the development of the SAFER HBM was prediction of rib fractures and brain injuries, as these injuries are the most common severe injuries for vehicle occupants. However, there is also a need to predict injuries to the lower extremities. Therefore, to enable prediction of femur fractures and knee joint injuries, detailed and validated models of the lower extremities are needed for the SAFER HBM.

1.1 Aim

The aim of this thesis is to develop and validate a FE model of the knee and femur, with connecting soft tissues, such as ligaments and tendons. The intention of the model is to increase the capability of the SAFER 50^{th} percentile male HBM to predict femur fractures and knee joint injury risk.

2
Background

In this chapter, basic anatomy of the knee and femur is described, geometrical and mechanical properties of the modelled parts are described, adequately validation test cases are presented and theory of methods used within this thesis is presented.

2.1 Anatomy

The lower extremity have two major functions: to support the weight of the body and to move the body in space [14]. It can be divided in three main regions: thigh, lower leg and foot. The thigh and the lower leg are connected by the knee joint. The thigh consists only of one bone, the femur, which is connected to the pelvic via the hip joint. The femur has three sections: the proximal end, the shaft and the distal end. Its proximal section is characterized by the spherical shaped head, which joints to the pelvis. In Figure 2.1 the planes normally used to describe the human body and the details of the femur are visualized.

The shaft is the longest section and constitutes the major part of the femur, see figure 2.1. The mid-shaft has a triangular cross-section. The anterior section of the femur is flat, the medial and the lateral corners are rounded, which forms a crest at the posterior section. This crest is called Linea Aspera. The distal section of the femur is characterized by its two large condyles, which are separated by the intercondylar fossa. The surface posterior and between the two condyles are grooved, and connects to the patella. The patella is a sesamoid bone, which is a bone formed within a muscle. The patella connects the tibia and the quadriceps femoris.

The lower leg consists of two bones, the tibia and the fibula. The tibia is the largest of the two and the one which bears the weight. The proximal end of the tibia is characterized by a plateau, a wide, and flat region, which contains the lateral condyle, the medial condyle and the intercondylar region in between the two condyles. The plateau of the tibia articulates to the distal end of the femur and forms the knee joint.

Bone tissue forms most of the adult skeleton and supports the weight of the body [15]. A bone is divided into cortical and trabecular bone tissues. The cortical bone tissue is the denser and stronger of the two, and forms the outermost shell [14]. The cortical thickness varies between and within bones. The cortical thickness of the femur varies between 1.0-1.5 mm at the distal and proximal ends to 3.9-9.7 mm at the mid-shaft [16]–[21]. The variation in thickness from the literature is due to the use of different data sets, specimens anthropometry or the direction of measurement. The maximum cortical thickness is found anteriorly of the mid-shaft [21]. Beneath the cortical bone at the distal and proximal end, the porous trabecular bone is found.

The main function of the knee is to allow for rotations between the thigh and the lower leg [14]. The knee consist of ligaments, tendons, bones, and cartilages. The major ligaments and tendons are: the Anterior Cruciate Ligament (ACL), the Posterior Cruciate Ligament (PCL), the Lateral Collateral Ligament (LCL), the Medial Collateral Ligament (MCL), the Patellar Tendon (PT) and the Quadriceps Tendon (QT) which are visualized in Figure 2.2. The cruciate ligaments prevent displacement of the tibia relative to the femur. The ACL prevents anterior displacement and the PCL prevents posterior displacement. The two cruciate ligaments forms a cross within the joint due to the attachment points. The ACL attaches at a facet at the lateral wall of the intercondylar fossa of the femur and the anterior part of the intercondylar region of the tibia. PCL attaches at a facet at the medial wall of the intercondylar fossa of the femur and the posterior part of the intercondylar region of the tibia.

The two collateral ligaments stabilize the hinge-like motion of the knee, and runs along the medial and lateral side of the joint. The MCL attaches at the medial femoral epicondyle and the medial surface of the tibia. The LCL attaches at the lateral femoral epicondyle and the lateral surface of the fibula head.

During the motion of the knee joint, the curvature of the two adjacent articular surfaces of the femur and tibia are changing. From flat contact, in standing posture, to round, in sitting posture. Therefore, two wedges and C-shaped menisci are located in between to compensate for the different contact surfaces and distribute the loads evenly during movement. The ends of the lateral and the medial meniscus attaches to the tibia plateau, they do not have any attachment to the femur. The lateral meniscus lateral face attaches to the joint capsule and to a branch of the MCL. The lateral and medial meniscus are connected via a transverse ligament anteriorly.

2.1.1 Cortical thickness

Many studies have been conducted throughout the years to measure and estimate the cortical thickness of the femur and tibia, the cortical thickness of the patella have been studied less. Most of the studies found focused on measuring the cortical thickness of the mid-shaft of the femur. The details of the studies vary, the most detailed studies have measured in different directions, e.g., anterior, posterior, lateral and medial direction, while the less detailed have not or only presents an averaged value of measured the directions.

Du et al. studied how the thickness of the femoral head and the femoral condyles varied, using clinical Computed Tomography (CT) [20]. A total of 95 samples were used in the study, both females and males of ages ranging from 16 to 83 years were

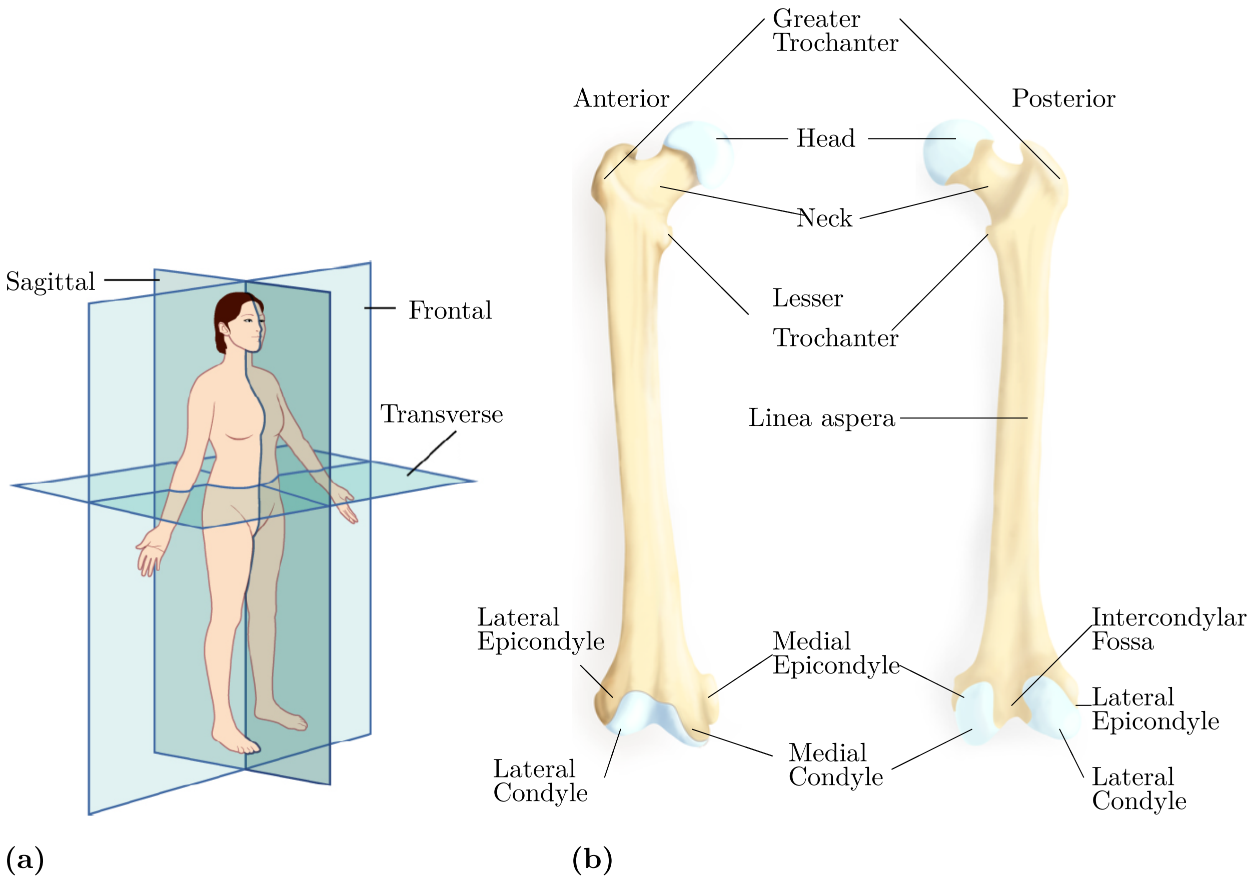

Figure 2.1: **(a)** The three planes normally used to describe a human, adjusted and extracted from [15], **(b)** details of the femur, adjusted and extracted from [22].

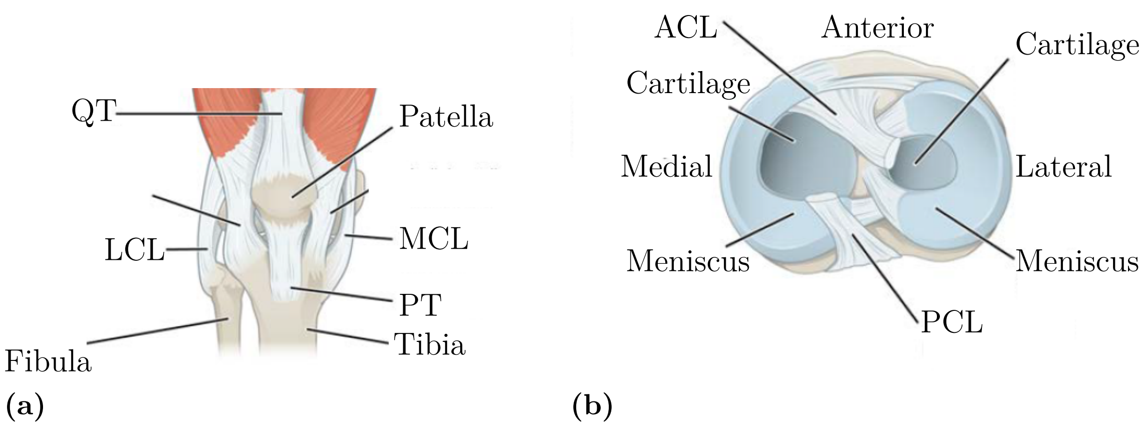

Figure 2.2: **(a)** anterior view of right knee, **(b)** superior view of right tibial plateau, adjusted and extracted from [15]

represented in the study. The samples were measured in the four directions described above. The study presents the results as a mean of the complete set, which limits the usefulness of the study, and the directions of measurements are vague. However, the study gives a guidance how the thickness of the cortical bone tissue varies in these two areas of the femur. The cortical thickness of the head ranges from 0.96-1.51 mm and 1.19-1.41 mm at the condyles.

Malo et al. measured the cortical thickness at two sections of the femur, the middle of the neck and the proximal shaft just below the lesser trochanter [23]. Only male samples were used and the mean of the anthropometric data corresponds to the 50^{th} percentile male, 47.1 years, 177.1 cm and 84.8 kg, the weight of the PMHS are above the average 50^{th} percentile male [2], [24]. The cortical thickness of the 21 samples were estimated using a scanning acoustic microscope equipped with an ultrasound transducer. Samples of the neck were cut perpendicular to the long axis of the neck and the average thickness was estimated to 1.6 mm, 1.3 mm, 1.7 mm and 2.8 mm in anterior, posterior, superior and inferior direction. Samples of the proximal shaft were cut perpendicular to the long axis of the shaft and the average cortical thickness was estimated to 5.0 mm, 4.6 mm, 5.6 mm and 6.4 mm in anterior, posterior, medial and lateral direction.

Ziopus et al. measured the maximum cortical thickness of cut specimens of the mid-shaft along AP and ML planes [19]. The mean cortical thickness of the measured specimen was 6.89 mm. The bones were harvested from ten male cadavers. The height and weight of the cadavers are below that of a 50^{th} percentile male, 166 cm and 66 kg, but corresponds in age 55 years.

Feik et al. investigated how the cortical thickness varied depending on sex and age [21]. 2-4 cm specimens of the femoral mid-shaft were cut. The cortical thickness was estimated using images captured of 100 µm thick samples of the specimens using microradiography. After the first cut, the directions of the specimens were not marked, so the medial and lateral aspects could not be identified. Thus, the thickness of the two aspects was lumped. The specimens included in the study were divided into sets depending on sex and age. Three age groups of 20-40, 41-60 and 60+ were used for the two sexes. The cortical thickness was measured to 6.11 mm, 9.02 mm and 7.79 mm in anterior, posterior and lateral-medial direction of the subset of males with an average age of 53 years and height of 171 cm. The cortical thickness was also found to be lower for the oldest age group compared to the other age groups.

Someya et al. had a similar research topic as Feik et al. [25]. The cortical thickness was estimated using 3D models based on clinical CT of 21 young humans. Twelve regions were identified on each femur, anterior, posterior, lateral and medial directions at three sections of the femur, distal 20-37%, mid 37-54% and proximal 54-71%. The length of the femur was defined as the length between the centre of the femoral head to the origin at the mid-point between the line connecting the centre points of the two femoral condyles. The cortical thickness of the distal, mid and proximal regions was measured to 5.5 mm, 6.3 mm, 5.5 mm, 5.5 mm; 6.8 mm, 7.8 mm, 7.1 mm, 7.4 mm; 6.7 mm, 7.8 mm, 7.3 mm and 7.2 mm in anterior, posterior, lateral and medial directions. Similar to the previous study, the cortical thickness decreased in the older age group compared to the younger.

Klein et al. created and validated statistical FE models of male and female femurs [26]. In order to create a statistical FE model of the male femur, 62 males, age ranging from 18-89 years, were CT scanned. The specimens were divided into five cross-sections along the long axis of the mid-shaft, and one cross-section of the neck region, section 0. Cross-section 1 and 5 were located at 25% of the total femur length from the distal and lateral end. Cross-section 2-4 were evenly spaced between section 1 and 5. The length of the femur was defined as the length along the long axis of the bone between the most superior and inferior points. At cross-section 1-5 the total and cortical cross-sectional areas were measured, while only the total cross-sectional area was measured at section 0.

2.2 Biomechanical properties

2.2.1 Bone

The density, 1.8-2.0 g/cm^3, of cortical bone is typically greater than the density, 1.0-1.4g/cm^3, of the trabecular bone [27]. The difference is because of the marrow filled cavities in the trabecular bone.

Bones are generally anisotropic due to its different components and composition. If considering the generalized Hooke's law, 21 components are needed to describe the mechanical properties of a fully anisotropic material. But according to Cowin and Martin, the properties are often simplified to orthogonal or transversely isotropic behaviour [27], [28] which reduces the 21 components to nine or six components.

Cowin and Martin have compiled mechanical tests of bone specimens conducted historically [27], [28]. The mechanical properties of the trabecular and cortical bone varies largely, due to age, composition, and direction. The transverse and longitudinal Young's modulus of the cortical bone varied between 11.5-18.8 GPa and 17.0-27.4 GPa [28], and the longitudinal yield strength varied between 115-133 MPa [27], [28]. The Young's modulus of the trabecular bone varied between 90-489 MPa according to four conducted tests [27].

Bayraktar et al. exposed specimens of femur from males and females to uniaxial tension at a strain rate of 0.2%/s to determine the elastic and yield properties of a human femoral bone [29]. The cortical bone specimens were cut longitudinal of the mid-shaft, obtaining 74 specimens. The average Young's modulus and yield strength were 19.9 GPa and 107.9 MPa, respectively. The average apparent density of trabecular bone tissue of the specimens were 0.62 g/cm^3.

Zysset et al. conducted 1401 hardness tests from 8 individual cadavers to estimate elastic modulus of the cortical and the trabecular bone [30]. Cortical bone specimens were extracted from the femoral mid-shaft and the elastic modulus were computed at the unloading force-displacement curve and assuming Poisson's ratio to 0.3. The average elastic modulus for the cortical bone was estimated to be 20.1 GPa.

Ziopus et al. estimated the elastic modulus to 16.4 GPa via three-point-bending of cortical femoral specimens [19]. The 30 cortical bone specimens were harvested from the femoral mid-shaft of ten male cadavers with age range of 35-90. The three-point-bending of the specimens were conducted according to the *ASTM D790-86* standard. Age had an influence on the elastic modulus, the elastic modulus tends to decrease with ageing.

2.2.2 Ligaments and Tendons

Ligament connects one bone to another and prevents relative motion between the bones [27]. E.g., the ACL connects the femur to the tibia and prevents anterior motion of the tibia relative to the femur, as mentioned in Section 2.1. Tendons connect muscles to bones. There are mainly two components of ligaments and tendons: collagen and elastin. The collagen are tightly packed bundles of crimped fibres with the principal direction aligned in the direction of force, which gives the tensile properties. The elastin fibres give the elastic properties. Ligament consists of more elastin than tendons and tendons consist of more collagen than ligaments, which makes ligament more elastic than tendons.

A typical load-strain curve, obtained as a result of tension test of a ligament or tendon, can be segmented into three parts, see Figure 2.3. First the toe region, where low forces are needed to elongate the ligament or tendon. In this region, the crimped collagen fibres are straightened to parallel fibres. Further loading, beyond 1.5-3% of strain, produces a linear segment of the load-strain curve. This part of the curve represents the stiffness of the ligament or tendon. Finally, the curve ends with a yield segment, where the loads are increased to a point where fibre damage occurs. Thus, the load capability of the ligament or tendon is reduced before it fails completely.

Ligaments and tendons are normally viscoelastic. The mechanical properties are rate and history dependent, the properties changes with deformation rate and previous deformations. Hence, test parameters used in tests must be well documented since it affects the result of the tests. Repeatedly loading of a ligament or tendon reduces the stiffness and increases the deformation of given applied load.

Orozco et al. conducted a study of the effect of the constitutive representations and the structural constituents of knee ligaments on joint knee mechanics [31]. Five different constitutive models were compared when evaluating the joint forces. The complexity level varied from defining the constitutive model, spring material formulation, with one parameter to six parameters, fibril-reinforced porohyperelastic

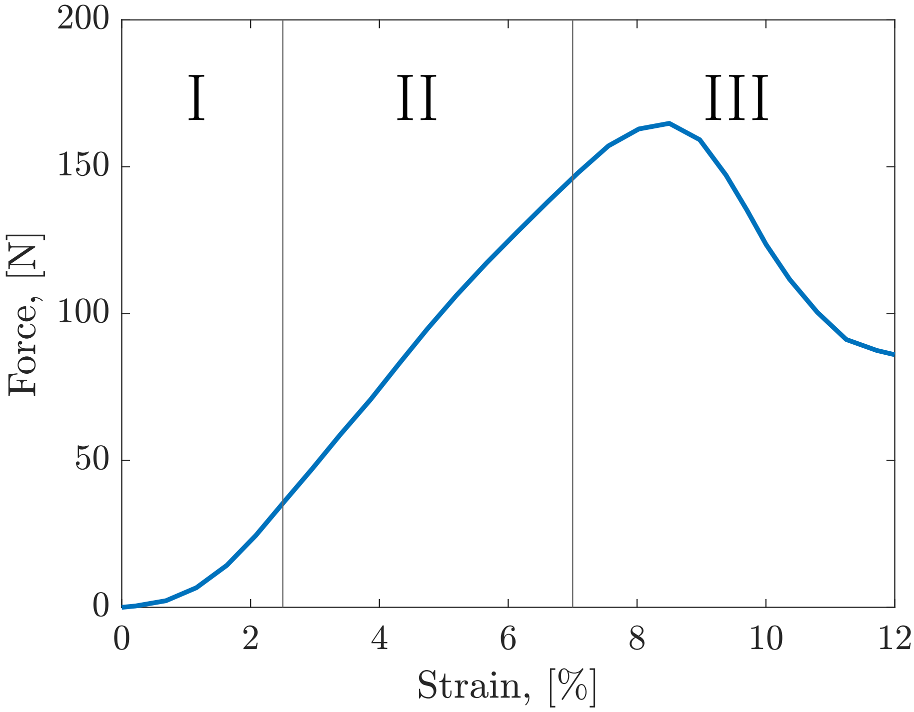

Figure 2.3: Typical load-strain curve of a ligament or tendon. Where I is the toe segment, II is the linear segment and III is the yield segment.

material. Their results indicate that models of less complexity can be used if the loading is applied along the ligaments long axis. They also conducted a literature review of the material properties. Based on 37 sources they determined the elastic modulus to 123 MPa, 168 MPa, 224 MPa, 280 MPa, 336 MPa and 370 MPa for ACL, PCL, MCL, LCL, PT and QT, respectively and the Poisson's ratio for all ligaments and tendon to 0.4.

Numerous studies have been conducted to describe the knee ligaments variations in shape and geometry. Researchers have used different methods, more classical methods like measurements of PMHS using calipers, and more modern methods like 3D models obtained of scanned objects.

Belvedere et al. studied how the length of the ligaments varied due to flexion angle [32]. Ten PMHS knees were analysed of varying age 3-92 and sex, six knees from male PMHS, using a 3D bone tracking device with an accuracy of 0.5 mm and 0.5°. The four major ligaments, and the PT, were analysed. The knee was flexed from 0° to 130° of flexion angle. The maximum length occurred at fully extension, i.e., 0° flexion angle, for all ligaments except the PCL. The maximum length of the PCL occurred at the region of 90°-130° of flexion angle. According to Belvadere the maximum length of the ligaments varied largely between the different bundles, 25.1-30.1 mm, 26.8-29.8 mm, 43.6-91.7, 48.0-50.7 mm and 57.5-66.0 mm for the ACL, PCL, MCL, LCL and the PT.

Otake et al. studied the morphology of the collateral ligaments of the knee [33]. 32

specimens were examined in full extension. The insertion points of the ligaments, the anterior and posterior length and the width of the insertion points were recorded using calipers. The centroids of the MCL femoral and tibial insertion point were located 27.7 mm posterior off the anterior margin of the medial condyle, 27.7 mm proximal to the inferior margin of the medial condyle and 23.1 mm posterior to the anterior margin of the tibia and 49.9 mm distal to the superior margin of the medial tibial plateau in the sagittal plane. The posterior length of the MCL was greater than the anterior 92.8 mm and 80.1 mm, respectively. The width of the femoral insertion point was greater than the tibial, 11.3 mm and 9.5 mm, respectively. The centroids of the LCL femoral and fibula insertion point were located 40.6 mm posterior to the anterior margin of the lateral condyle, 22.9 mm proximal to the inferior margin of the lateral condyle and 13.0 mm posterior to the anterior margin of the fibula head, 25.3 mm distal to the superior margin of the lateral tibial plateau in the sagittal plane. The posterior length of the LCL was greater than the anterior 52.9 mm and 54.6 mm, respectively. The width of the femoral insertion point was greater than the fibula, 8.8 mm and 6.8 mm, respectively.

Harner et al. studied how the size and shape of the cruciate ligaments varied within eight PMHS knees [34]. The measurements were made at five levels of each ligament at four flexion angles, with a laser micro meter micrometer system. The cross-sectional shape of cruciate ligaments is best describes as irregular, i.e., not purely circular or elliptical. The knee joint flexion angle did not have a significant effect on the cross-section, but the shape of the cross-section altered with the knee joint flexion. The cross-section of the ACL and PCL varied along its length 48-51 mm^2 and 35-43 mm^2, respectively, at a knee flexion angle of 30°.

Harner et al. conducted a data collecting study on the insertion sites of the cruciate ligaments [35]. The five specimens were analysed using a laser micrometer system at 30° flexion angle. The cross-section of the insertion points were 3-3.5 times larger than the mid-substance. Cross-section areas of the ACL's femoral and tibial insertions were 113 mm^2 and 136 mm^2, respectively, and 34 mm^2 at the mid-substance. Cross-section areas of the PCL's femoral and tibial insertions were 128 mm^2 and 153 mm^2, respectively, and 49 mm^2 at the mid-substance.

Zheng et al. studied the insertions of the soft tissues to the tibial plateau as well as the interrelationship between the insertions[36]. 20 3D bone models were generated from CT-scans of 20 PMHS tibias. Principal component analysis was used to provide geometrics between the scanned plateaus. The insertion cross-section areas of the ACL and PCL were 115 mm^2 and 79.9 mm^2, respectively. The shape of the insertion cross-sections are best described as irregular. The interrelation 2D distance between the two cruciate insertion points was 26.6 mm.

2.3 Explicit and Implicit FEM

The finite element method (FEM) is a numerical approach to solve differential equations approximately [8], which can be used to solve a variety of engineering problems. Instead of seeking approximations of the differential equation of the entire region, the region is discretized into smaller elements, *finite elements*, and the approximations are carried out over each element [8]. Then the elements are assembled to form the initial region. The dynamic equilibrium equation in matrix form (2.1).

$$\boldsymbol{M}\ddot{\boldsymbol{u}}^n + \boldsymbol{C}\dot{\boldsymbol{u}}^n + \boldsymbol{K}\boldsymbol{u}^n = \boldsymbol{f}^n \tag{2.1}$$

where $\boldsymbol{M}, \boldsymbol{C}$ and $\boldsymbol{K}$ are the mass, damping and stiffness matrix respectively and $\boldsymbol{u}$ and $\boldsymbol{f}$ are the displacement and load vector, respectively. n denotes the number of discretized time step $t \in [t_0, t_0 + \Delta t, t_0 + 2\Delta t, ..., t_0 + n\Delta t]$.

To solve (2.1) different techniques can be used. Two of the main techniques are implicit and explicit time integration. Solving it implicitly is computationally more costly than solving it explicitly, since the implicit analysis requires matrix inversion at each time step, which are costly. Explicit analysis does not require this step. To highlight the difference between the explicit and implicit solving technique of (2.1), the different approaches are:

$$\boldsymbol{u}^{n+1} = f(\boldsymbol{u}^n, \dot{\boldsymbol{u}}^n, \ddot{\boldsymbol{u}}^n, \boldsymbol{u}^{n-1}, \dot{\boldsymbol{u}}^{n-1}, \ddot{\boldsymbol{u}}^{n-1}, ...) \tag{2.2}$$

$$\boldsymbol{u}^{n+1} = f(\dot{\boldsymbol{u}}^{n+1}, \ddot{\boldsymbol{u}}^{n+1}, \boldsymbol{u}^n, \dot{\boldsymbol{u}}^n, \ddot{\boldsymbol{u}}^n, ...) \tag{2.3}$$

whereas (2.2) is the explicit approach and (2.3) is the implicit. The explicit approach is only depending on preceding steps, while the implicit approach depends on the current and preceding steps. Hence, the implicit technique requires iterative steps to establish equilibrium. This makes it more computationally costly than solving it explicitly.

If solving explicitly, compared to implicitly the number of time steps are increased 100-10000 times [37]. Solving it implicitly requires less, but more expansive time steps. When solving explicitly, the time steps are limited by the critical time step, $\Delta t_{critical}$, defined as the element length, l_e, divided by the wave propagation in an element, c_e. The wave propagation, c_e, for a solid element are defined as:

$$c_e = \sqrt{\frac{E(1-\nu)}{(1+\nu)(1-2\nu)\rho}} \tag{2.4}$$

where E is the Young's modulus, ν is the Poisson's ratio and ρ is the density of the element. To satisfy the critical time step, two main parameters can be adjusted, the stiffness and the density. In elements where the critical time step is not satisfied, additional mass can be added, by increasing the density of the element, so it satisfies the critical time step. However, when adding mass to a model, it may affect the result. To not affect the result drastically, the added mass must be controlled.

2.3.1 Mesh quality

It is of great importance that one can trust the results of simulations using the generated FE models. To ensure trustworthiness and stable simulations, the mesh must be of good quality. The generated mesh within this project must fulfil the quality criteria stated in appendix K in [38]. All elements of the mesh must fulfil the 100% requirement, which are requirements of the aspect ratio, skewness, warpage, internal angles and Jacobian which are tabulated in 2.1 and illustrated in Figure 2.4.

The aspect ratio of an eight node solid element is defined as the ratio of the maximum width related to the minimum width of the element. It is calculated as: $AR = \frac{\max(h_1)}{\min(h_i)}$ for $i = 1, 2, 3$, where h is the width of the element.

The skewness is an angle measure of how close the element is to an ideal element. The skewness is calculated as: $Skew = 90 - \min(\varphi_i)$ for $i = 1, 2$, where φ are the angles between the two lines connecting the mid-points of opposite sides in each facet of the element.

Warpage is a measure of how far off the element is of being planar. The warpage is calculated as: $\theta_i = \max(\arcsin(\frac{a_i}{l_i}))$ for $i = 1, 2, 3, 4$, where θ is the warping angle, a is the distance between the reference node of the ideal planar facet to the node of the element facet and l is the distance from the mid-point of the facet to the reference node of the ideal planar facet. This is done for each node of the six facets, and the maximum is retained as the warping angle.

Hexa angle is an angle measure between two neighbouring facets. ψ_i for $i = 1, 2, ..., 12$, where ψ is the hexa angle, between two facets.

Jacobian is the determinant of the Jacobian matrix, and it is a measure of the distortion of the element. The Jacobian matrix relates an ideal unit cube in the parent domain to the global domain. A perfectly cubically shaped element have the Jacobian of 1.

The draft states that the added mass must be below 5% for each part. But it does not define the meaning of part. E.g., a part could the femur or the thigh (including femur, fat, skin, and other soft tissues) Therefore, 5% of added mass will be interpreted as a guideline, not a requirement.

Table 2.1: SAFER HBM mesh quality criteria

	Aspect ratio	**Skewness**	**Warpage**	**Hexa Angle**	**Jacobian**
	[-]	[°]	[°]	[°]	[-]
Method	Patran	Patran	Patran	Abaqus	ANSA
Solids	<10.0	<60	<20	20<ϕ<160	J>0.3

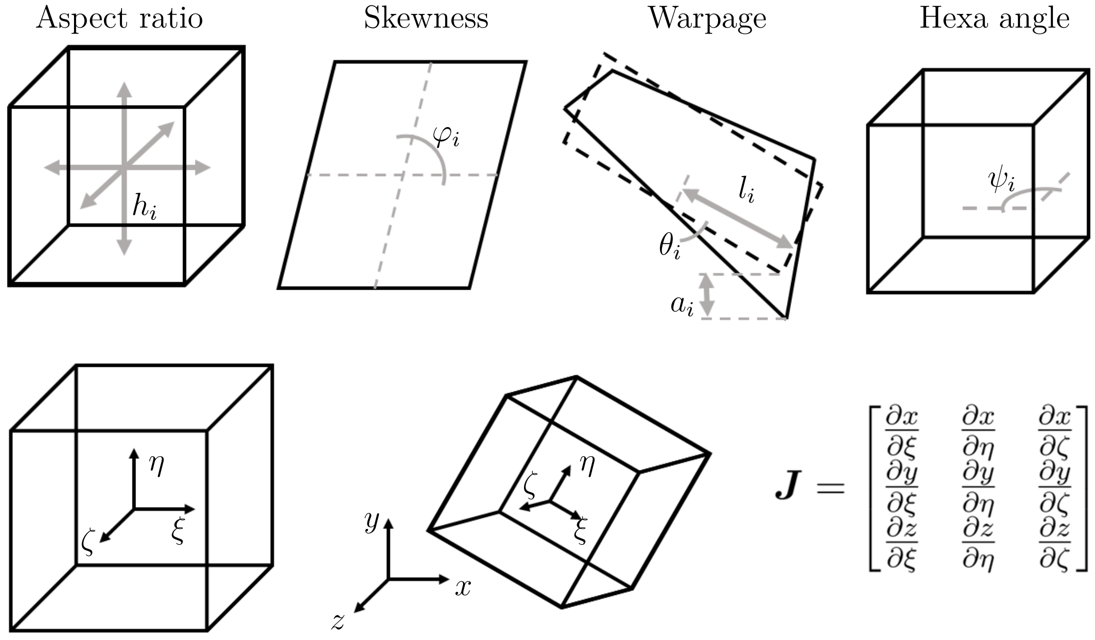

Figure 2.4: Illustration of the element quality criteria, Aspect ratio, Skewness, Warpage and Hexa angle, and of the distortion with belonging Jacobian matrix.

2.4 Validation

A literature review was conducted to find experiments and tests that could be used for validation of the femur and knee joint in kinetic and kinematic sense. Three main databases were used to find literature: *Scopus*, *Google Scholar* and *Chalmers library.* Several keywords and combinations were used, *mechanical, structural, properties, fracture, impact, bending, tension, femur, knee, ligament, collateral, cruciate, etc.*

For a paper to be used as a validation reference, it must fulfil some criteria. It must include a detailed description of the boundary conditions, a record of in-data (e.g., load-path curves), well documented data of the specimens used in the paper, and finally the result of the paper must be presented adequately. E.g., papers only presented the final results as the ultimate values, without time history plots, are hard to replicate.

2.4.1 Loading of the Femur

Eight femur loading studies were found during the literature review. Five of them studied the response of the femur exposed to dynamic three-point-bending [39]–[43]. One, [43], included two additional load cases, axial compression and a combined load case of three-point-bending and axial compression. Three of them studied the response of the femur exposed to quasistatic compression of the femoral head [44]–[46]. Major details of the test series are tabulated in Table 2.2. Data presented in the table are the average of the male specimens if applicable, else the average of all specimens are tabulated. The moment, force, and deflection values are the average of the maximum values occurring during the tests, i.e., ultimate values.

Funk et al. exposed 15 denuded femurs from male PMHS to posterior-anterior (PA) and lateral-medial (LM) three-point-bending [39]. The ends of the femur, approximately 8 cm, were potted in a polyurethane foam and then placed on two rolling supports. The contact surface between the rolling supports and the triaxial load cell was greased to reduced shear and moments. The mid-length of the femur was impacted by a ∅12 mm cylinder at a constant speed of 1.2 m/s until the femur was fractured. During the test, the reaction load and the strain at the opposite side of impact was recorded. The bending moment was determined by averaging the reaction loads and multiplied by the distance to the centre of the femur. Funk et al. presents ultimate values and a typical load-path curve of one specimen as results of the tests.

Kerrigan et al. exposed 8 denuded femurs to LM three-point-bending [40]. 10.2 cm of the bone ends were potted in polyurethane foam and placed on rolling supports with the medial side down. The contact surface between the rolling supports and the triaxial load cell was greased. They impacted the femurs at three different locations, mid-length and 1/3 of the length from the distal and proximal ends. The femurs were impacted by a ∅12.7 mm steel cylinder embedded in 25 mm thick foam at the average speed of 1.2 m/s until the impactor reached a displacement of 90 mm. The intention of the foam was to represent the soft tissues of the thigh, i.e. the fat, muscle and skin tissue. The bending moment was calculated at the impact location from the two supports and then averaged. Kerrigan et al. presents ultimate values and a typical load-path curve of one specimen as results of the tests.

Forman et al. exposed 16 denuded femurs to medial-lateral (ML) three-point-bending [41]. The bone ends were potted in two-part polymer blocks and placed on rolling supports. The ends were positioned such that the centre of the femoral head and the distal femoral notch lined up, and the load was applied perpendicular to this line. The contact surface between the rolling supports and the 6-axis load cells was greased. The mid-length of the femurs was impacted by a ∅13 mm ram embedded in a 25 mm thick foam at a constant speed of 1.5 m/s. The bending moment was calculated as:

$$M = \frac{LF_1F_2}{F_1 + F_2} \tag{2.5}$$

where L is the length between rolling supports and F_1 & F_2 is the vertical reaction loads recorded at the two load cells. Forman et al. presents ultimate values as results of the tests. The intention of Forman et al. study was to capture mechanical factors contributing to fracture tolerance throughout skeletal development, thus the age span of the specimen is ranging from 1 to 57 years of age. Specimens below the age of 18 years are excluded from this paragraph and Table 2.2.

Kennedy et al. exposed 45 femurs to PA and LM three-point-bending [42]. The soft tissues were kept, except at the ends. The denuded ends were potted in rigid rectangular mounts using filler. The potted ends were placed on semi rectangular roller supports. The contact surface between the rolling supports and the load cell was greased. A ∅35 mm impactor with a mass of 9.8 kg was dropped on the specimen from a height of 2.2 m, resulting in an impact velocity of 5 m/s. The bending moment was calculated in two ways, one using the reaction load cells, M_I (2.6), and one from the impactor load cell, M_R (2.7).

$$M_I = (\frac{F_{IMP}}{2})(\frac{L}{2}) = (\frac{F_{LR} + F_{RR} + ma}{2})(\frac{L}{2}) \tag{2.6}$$

$$M_R = (\frac{F_{LR} + F_{RR}}{2})(\frac{L}{2}) = (\frac{F_{IMP} - ma}{2})(\frac{L}{2}) \tag{2.7}$$

Here, F_{IMP} is the load recorded by the impactor load cell, F_{LR} & F_{LR} is the load recorded by the reaction load cells, ma is the inertial term which represents the inertia of the effective mass from the linear acceleration during impact and L is the length between the two supports. Due to the inertial term, (2.6) will overestimate the bending moment and (2.7) will underestimate the bending moment. Kennedy et al. presents ultimate values of all specimens and typical load-path curves of selected specimens as results of the study.

Keyak et al. exposed 32 denuded femur heads to compression in two different directions, one to replicate the stance phase of gait and one to replicate an impact from a fall [44]. The distal end was removed, approximately 2/3 of the total femur length was kept, and the distal shaft was embedded in polymethyl methacrylate (PMMA). The embedded part of the shaft was constrained. To minimize local stress concentrations to the head and greater trochanter, in the fall condition moulded PMMA cups were used. The specimens were tested until failure. Keyak et al. presents ultimate loads as result from the tests.

Cody et al. exposed 51 denuded femurs heads to compression, replicating the single stance phase of gait [45]. The femurs were cut approximately 14 cm distal of the mid-point of the lesser trochanter. The cut specimen was placed in an aluminium fixture with PMMA. The load was applied in a quasistatic manner, using a displacement rate of 0.21 mm/s at the head, and the load was applied until failure. Cody et al. presents ultimate loads for all specimens.

Bessho et al. exposed 11 denuded femur heads to compression in a stance phase [46]. The femurs were cut 14 cm distal of the mid-point of the lesser trochanter. 5 cm of the remaining shaft was embedded in wood metal and constrained by a support during the test. A resin cap was placed on the femoral head to distribute the load uniformly. The compression load was applied in a quasistatic manner, using a displacement rate of 0.5 mm/min, until fracture. Bessho et al. presents ultimate loads for all specimens and load-path curves for selected specimens as results of the tests.

Ivarsson et al. exposed 47 denuded femurs shafts to AP and PA three-point-bending, axial compression and a combination of them two. The ends of the femurs were removed, the cut ends were potted in aluminium cups using urethane resin. The cups were placed in cup holders which only allowed rotation in the plane of the set-up. A ⌀25.4 mm aluminium impactor embedded in 6.2 mm foam impacted the mid-shaft at a constant speed of 1.5 m/s until 72 mm stroke of the actuator. In the combined case, the axial compression was 0.263 mm per 1 mm of displacement of the impactor. Ivarsson et al. presents ultimate values of all specimens and load-path curves of all specimens as result from the tests.

Ivarsson et al. research in 2009 [43] fulfils the criteria, described in Section 2.4. It was the validation reference which satisfied the criteria the best and the only paper found which described the in-data satisfactory. Thus, it will be used as the validation of the femur FE model.

2.4.2 Loading of the Major Ligaments

In total, the nine studies describing the response of the major ligaments exposed to tension found during the literature study are described below. In Table 2.3 the major details of the papers are tabulated.

Van Dommelen et al. exposed ligaments from eight male PHMS to dynamic tension load [47]. All the four major ligaments of the knee were tested in this study. All the soft tissues were removed except for the ACL or the PCL and the collateral ligaments. Each ligament was separated with bone ends kept, creating bone-ligament-bone (BLB) samples. The ACLs and the PCLs were split into two bundles, anteromedial and posterolateral bundle and anterolateral and posteromedial bundle, respectively. The BLB specimens were mounted anatomically and tested in a biaxial test machine. Before the test, the specimen was preconditioned with 240 cycles of sinusoidal displacement at 8 Hz to a relative elongation of 8%. Then it was subjected to the testing scheme described in the study. In the last step of the test scheme, the specimen was tested until failure at different velocities. During the test, the reaction load was recorded using a six-axis load cell. Van Dommelen et al. presents ultimate loads and load-path curves for all tested specimens and corridor values of load-path curves as the result of theirs study.

Jones et al. exposed 28 ACLs to tension load [48]. All the soft tissues were removed except the ACL, and approximately 150 mm of the tibia and femur were included. The bone ends were placed in a rig that constrained the knee to 30° degrees of flexion. Before the test, the specimens were preconditioned of five loading-unloading cycles up to 50% of the body weight. The load was applied to the tibia, in a manner to simulate the tibia to be drawn anteriorly relative to the femur. Then they were loaded until failure at the speed of 500 mm/min. Jones et al. presents ultimate load and a typical load-path curve as the result from the tests.

Table 2.2: Compilation of major details in femur validation papers. The data in the table are the mean of all male specimens if applicable, else the mean of all specimens are tabulated.

Paper	Type	Samples [No.]	Sex [No.]	Age [year]	BC	Results
Funk [39]	3-pt	15	15,0	59	Rolling	Failure data
Kerrigan [40]	3-pt	8	2,6	60	Rolling	Failure data, Load curves
Forman [41]	3-pt	16	15,1	24	Rolling	Failure data
Kennedy[a] [42]	3-pt	45	mixed	65	Rolling	Failure data, Load curves
Keyak [44]	Comp.	32	mixed	71	Fixed	Failure data
Cody [45]	Comp.	51	28,23	42-93	Fixed	Failure data
Bessho [46]	Comp.	11	5,6	57,72	Fixed	Failure data, Load curves
Ivarsson [43]	3-pt, Ax. Comp, Comb	47	27,20	55	Rolling	Failure data, Load curves

Paper	Direction	Speed [m/s]	Moment [Nm]	Force [N]	Deflection [mm]
Funk [39]	PA, LM	1.2	458	4349	17.6
Kerrigan [40]	LM	1.2	412	4346	20.6
Forman [41]	ML	1.2	496	-	-
Kennedy[a] [42]	LM, PA	5[b]	352, 348	4180, 378	-
Keyak [44]	S/F	-	-	8400, 2300	-
Cody [45]	S	Q	-	9496	-
Bessho	S	Q	-	5432	-
Ivarsson[c] [43]	PA, AP	1.5	454	7599	9.9
Ivarsson[d] [43]	PA,AP	1.5	374	-	10.0
Ivarsson[e] [43]	Axial	1.5	-	25546	11.0

[a]Specimens with ages below 18 are excluded, [b]impact speed, [c]combined load case, [d]three-point-bending, [e]axial compression
S- stance configuration, F- fall configuration, Q- quasistatic loading, speeds below 0.05 m/s, Force is the reaction force between impactor and specimen except for Ivarsson test where Force is the axial force in the specimen, Sex is presented as Males, Females.

Woo et al. exposed 27 ACLs to Anterior-Posterior (AP) displacement controlled tests and tension tests in two orientations, anatomical and tibial orientation [49]. Before testing the ACL to failure, an AP displacement test was conducted to quantify the ACL's contribution to the stability of the knee. For the AP displacement test, the knee was dissected free from all skin and muscle tissue, removed the patella and leaving the joint capsule intact with all ligaments intact. After the AP displacement test, the remaining soft tissues were removed except the ACL. The tensile test was conducted in two different orientations, anatomical and tibial orientation. For the anatomical orientation, the specimen was placed to keep the anatomical position of the knee and the tensile load was applied in the long axis of the ACL. For specimens tested in the tibial orientation, the tensile load was applied along the long axis of the tibia. Both the tests were conducted with a knee flexion angle of 30° degrees. Woo et al. presents ultimate fail loads, a typical load-path curve and averaged load-path curves as their result. The authors claimed that both the age and the orientation of the specimen had a significant effect on the mechanical properties. The stiffness, ultimate load and the absorbed energy reduces with age, and anatomical orientation was more beneficial than tibial orientation.

Paschos et al. exposed ten ACLs to tension load [50]. The knees were dissected free of all soft tissues except the ACL. Before the tension test, measurements of the ACL were taken. One transverse hole was drilled in the femur and the tibia. The knees were placed in the test machine with 15° flexion angle and the ACL axis was aligned with the load axis. The tibia and femur were then aligned with the axis of ACL to prevent rotation variations. The femur and tibia were constrained from moving horizontally and vertically by use of two pins mounted through each bone. To prevent rotation about the pins, the bones were secured with a special designed square nut. No precondition was applied to the specimens before the failure test. The ACL was then loaded until failure at a displacement rate of 1.5×10^{-3} m/s. Paschos et al. presents ultimate loads and load-path curves for all tested specimens as results of their study. They also estimate Young's modulus by assuming a circular cross-section of the ACL.

Balasubramanian et al. exposed 14 knees at 90° flexion angle to an AP motion of the tibia [51]. Three series of tests were conducted, series I with intact knees, series II with knees dissected free from all soft tissues except the PCL and removing the patella and fibula and last series III with knees similar to series II but with an additional fixture to prevent tibial bending fracture. For all the three test series the femur and tibia (and fibula, for series I) were cut approximately 152 and 127 mm, respectively, from the centre of the lateral femoral condyle. The soft tissues were removed from the cut ends and potted in resins pot holders. The femoral pot holder was fixed in the test fixture, then the tibial pot holder was placed on a sled with approximately 90° flexion angle. Specimens in series II and III were placed more arbitrary based on visuals due to lack of stability of the dissected knee joint. The sled was then accelerated to a target speed of 1.8 m/s with a stroke length of 75 mm or more to ensure failure. Balasubramanian et al. presents ultimate load and load-path curves for all tested specimen as results of their study.

Harner et al. exposed 14 PCLs to uniaxial tension load [52]. All soft tissues except the PCL were removed from the specimens, and the PCL was separated into two bundles, anterolateral and posteromedial. The femur end was potted in PMMA and the tibia end was fixed in an aluminium cylinder using five bolts. The specimen was then clamped in the test machine, which aligned the PCL so that uniaxial load could be applied along the ligament axis. Before the specimen were tested to failure, they were preconditioned for 10 loading-unloading cycles up till 2 mm extension at 10% of the failure load speed. Then the specimen was uniaxial tensioned to failure at 3.33×10^{-3} m/s. Harner et al. presents average ultimate loads and a typical load-path curve as results of their study. The anterolateral bundle have a 3-4 times larger ultimate load than the posteromedial bundle.

Cho et al. exposed 21 MCLs and LCLs to tension load [53]. They kept approximately 50 mm of respective bone, the tibia, and fibula were articulated, and the tibia was split in the mid-sagittal plane. Each bone end was then potted in PMMA cups. The femur was fixed in the test machine and the tested ligament cup was fixed so that uniaxial load was applied to the long axis of the specimen. The ligaments were tested to failure at 1.67×10^{-3} m/s. Cho et al. presents average ultimate loads and a typical load-path curve as results of their study. The MCL reached a larger ultimate load than the LCL. They also estimate the Young's modulus by assuming a rectangular shape of the MCL and an oval shape of the LCL.

Kerrigan et al. exposed six MCLs and seven LCLs from male PMHS to tension load [54]. The intention of their study was to examine how the loading rate affects the specimen's properties. All soft tissues except for the major ligaments were removed from the specimen. The location and the orientation of the insertions were recorded to be able to reproduce the orientation during testing. Then the fibula and tibia were articulated and cut 4-6 cm distal to the MCL and LCS insertion sites. The femur and the tibia were bisected in the mid-sagittal plane. Then the bone ends were potted in aluminium cups using urethane casting resin. The cups were clamped in the test machine accordingly to the recorded orientation. Before testing to failure, the ligaments were preconditioned during 40 load-unload cycles to maximum 10% strain. The failure test was conducted at 1.6×10^{-3} m/s and 1.6 m/s. Kerrigan et al. presents ultimate loads and load-path curves for all tested specimens as results of their study. The stress level is greater at a particular strain for the greater test speed. They also estimate the Young's modulus of the specimens based on a scanned cross-section of the specimen. The average ultimate stress of the LCL is more than double the ultimate stress of the MCL.

Robinson et al. exposed MCLs to tension load [55]. All soft tissues except the MCL were removed and approximately 200 mm of the femur and tibia were kept. The MCL was split into two bundles, superficial and deep bundle. The superficial bundle has insertion points at the femur and tibia, and the deep has an additional insertion point to the medial meniscus. The bone ends were potted in steel cylinders using PMMA. The tibia was fixed in the test machine, then the femur end was aligned so that the fibres in the bundle were evenly loaded, which correspond to a flexion angle of approximately 20°. Before loading to failure, the specimens were loaded between 1 N and 40 N at the speed of 1.67×10^{-4} m/s. After preconditioning, the specimens were loaded to failure at 1.67×10^{-2} m/s. Robinson et al. presents ultimate loads of all tested specimens and a typical load-path curve as their result of the study. The superficial bundle endured a greater ultimate load than the deep.

2.4.3 Loading of the Lower extremity

Once the body parts have been validated individually, the complete modelled lower extremity can be validated.

Rupp et al. exposed the knee-thigh-hip (KTH) complex of 22 PMHS, 15 males, to knee impacts, to investigate how the fracture tolerance of the hip varied with different postures of an occupant in a vehicle [56]. The lower extremity, including the pelvic, was positioned in three postures, neutral, 10° adducted and 30° flexed. The soft tissues were removed from the iliac wings and the pelvic was fixed to the test apparatus. The lower extremity was then impacted by a ram at the knee, in the direction of the long axis of the femur, at 1.0 to 1.2 m/s. The applied force was measured using a load axis between the ram and the impact location. The average fracture tolerance was 6.1 kN in neutral posture, and decreased for the 10° adducted and 30° flexed posture.

Rupp et al. exposed five male PMHS to knee impacts of a 255 kg accelerated platform [57]. A number of tests were conducted on these five male PMHS, with various speeds, 1.2, 3.5, 4.9 m/s, and various conditions, whole body, connections of thigh flesh to pelvis cut, thigh flesh removed, thigh flesh removed with a load cell implanted in the proximal femur and torso removed. The PMHS was seated on a greased bench and the torso was held by straps until 20 ms prior to impact, when the torso was released. The knees were then loaded by the accelerated mass and the load was aligned with the long axis of the femurs. The force was measured by load cells located between the impactors and the platform. The averaged maximum peak force, 6.02 kN, was obtained when exposing the whole body to a platform speed of 4.9 m/s.

Bose et al. exposed eight knees from male PMHS to LM four-point bending and eight knees from males to combined loading of LM three-point-bending and shearing [58]. The tibia and fibula were cut approximately 5 cm distal to the MCL insertion, and the femur approximately 5 cm proximal to the joint capsule. Approximately 5 cm of the bone ends were then dissected free from soft tissues to enable potting. The pots were mounted on horizontal bars which were connected via bearings, which allowed low friction rotation, to vertical support pillars. One of the ends were allowed to translate, hence simply supported boundary conditions were achieved. For the four-point-bending test, the bars were loaded by a fork. For the combined loading, the load was applied by an impactor at one of the bars. The most frequently dam-

Table 2.3: Compilation of major details of the major ligaments' validation papers. The data in the table are the mean of all male specimens if applicable, else the mean of all specimens are tabulated.

Paper	Ligament	Samples [No.]	Sex [No.]	Age [year]	Results
van Dommelen [47]	ACL	7	8, 0	53	Failure data, Load curves
Jones [48]	ACL	28	-	67	Failure data, Load curves
Woo [49]	ACL	27	12, 15	22-97	Failure data, Load curves
Paschos [50]	ACL	10	5, 5	74	Failure data, Load curves
Balasubranabian [51]	PCL	14	10, 4	66	Failure data, Load curves
van Dommelen [47]	PCL	2	8, 0	53	Failure data, Load curves
Harner [34]	PCL	14	-	52	Failure data, Load curves
van Dommelen [47]	MCL	11	8, 0	53	Failure data, Load curves
Cho [53]	MCL	21	9, 12	77	Failure data, Load curves
Kerrigan [54]	MCL	6	6, 0	55	Failure data, Load curves
Robinson [55]	MCL	8	-	78	Failure data, Load curves
van Dommelen [47]	LCL	11	8, 0	53	Failure data, Load curves
Cho [53]	LCL	21	9, 12	77	Failure data, Load curves
Kerrigan [54]	LCL	7	7, 0	55	Failure data, Load curves

Paper	Ligament	Speed [m/s]	Force [N]	Strain [-]
van Dommelen [47]	ACL	1.6	1000	0.2
Jones [48]	ACL	Q	1041	-
Woo [49]	ACL	Q	1503	-
Paschos [50]	ACL	Q	400	-
Balasubranabian [51]	PCL	1.8	1400-4000	-
van Dommelen [47]	PCL	1.6	650	0.16
Harner [34]	PCL	Q	1120	-
van Dommelen [47]	MCL	Q-1.6	1400	0.39
Cho [53]	MCL	Q	498	-
Kerrigan [54]	MCL	1.6	1214	0.11
Robinson [55]	MCL	Q	534	-
van Dommelen [47]	LCL	Q-1.6	540	0.18
Cho [53]	LCL	Q	263	-
Kerrigan [54]	LCL	1.6	571	0.10

[a]Specimens with ages below 18 are excluded, [b]impact speed, [c]combined load case, [d]three-point-bending, [e]axial compression

Q- quasistatic loading, speeds below 0.05 m/s, Force is the reaction force between impactor and specimen except for Ivarsson test where Force is the axial force in the specimen, Sex is presented as males, females.

aged part in the tests was the MCL. The load of the two tests was applied at a rate of 450 mm/s.

Similar to Bose work, Kerrigan exposed two knees from male PMHS to LM four-point-bending and two knees from male PMHS to LM shear [40]. Approximately 30 cm of the lower extremities were kept. The bone ends were dissected free of soft tissues for potting. The pots were affixed to load cells before it was mounted in the test apparatus. The knee was mounted on metal box rollers for the four-point bending test. The rollers were only allowed to translate in the direction of the long axis bone. Then a fork applied load at 600 mm/s to the rollers. The knee was mounted on metal boxes for the shear test. The load was applied vertically to the box mounted on the tibial bone end at 1.1 m/s. At the femoral bone end, the box was attached to a piston which loaded the knee in axial tension of constant force of 750 N.

2.5 Post-processing measures

To evaluate if the result of the simulations correlates to the result of the tests, two different methods will be used. One using statistically computed corridors and one curve to curve comparison.

2.5.1 Statistical corridors

To evaluate if the results from simulations correlates to test results, a statistical approach will be used. The approach of standard deviations will be used, which is a measure of the variation within the data set. The average, μ, and the standard deviation, SD, of the data set are calculated from test results from the same test setup, but with different specimens. Then the simulation results will be compared to the corridors of $\pm 2SD$. The standard deviation is calculated as the sample standard deviation:

$$SD = \sqrt{\frac{\sum(x_i - \mu)^2}{n-1}} \tag{2.8}$$

where x_i is the observed value of a sample, n is the number of observed samples and $i = 1, 2, ..., n$.

2.5.2 CORrelation and Analysis

To evaluate and objectively quantify how two curves correlates, e.g., time-history result from the tests and the simulations, the curves can be compared using the method of CORrelation and Analysis (CORA). It compares curves using two main methods, the cross-correlation and the corridor method [59]. The intention of using the CORA methodology is to quantify the correlation of the time-history results between the tested specimens and the simulations in an objective sense.

The corridor method ranks how well the comparison curve correlates to two corridors, inner and outer, based on the reference curve. The width of the inner corridors are based on the parameters Y_{norm}, a_o and the width of the outer corridors are based on b_0. The method ranks the correlation between 0, no correlation, and 1, perfect correlation. If the comparison curve lays within the inner corridor, the result is 1 and 0 if it is outside the outer corridor. If the comparison curve lays within the outer corridor but outside the inner corridor, the result interpolates linearly between 1 and 0.

The cross-correlation method ranks how a curve correlates to a reference curve by three metrics: progression, phase and size. The result from each metric ranges from 0 to 1, where 0 corresponds to no correlation and 1 to perfect correlation. Before calculating the three parameters, the reference curve is shifted in time by multiple time steps, within the limits of the parameter INT_{min}. This is done to compensate for the poor calculations of the corridor method if there is a time shift between the curves. Lastly, the metrics are computed based on the maximum allowed movement of the reference curve. The three parameters are weighted as 1/2, 1/4, 1/4 for the progression, phase and size.

The final result of the CORA evaluation is a 50/50 weighted result of the corridor and the cross-correlation method, ranging from 0 to 1.

3
Methodology

In this chapter, the methodology of the project will be presented. *ANSA* version 22.1.0 was used as pre-processor, *LS-DYNA* version 11.1.0 was used as FE solver and *META* version 22.1.0 was used as post-processor.

3.1 Geometry

The developed knee-femur model should represent the 50^{th} percentile male, but the available geometry model is based on a CT-scan of a 50^{th} percentile female. Hence, the female geometry model were scaled to represent the target population of 50^{th} percentile male. The geometry models, consisting of femur, patella, tibia and fibula, were imported into the 50^{th} percentile male occupant version of SAFER HBM v10 and aligned accordingly to the existing femur, and then the models were scaled 10% in each direction to fit the 50^{th} percentile SAFER male model. After the geometry models were scaled, the geometry of the tibia and fibula were rotated in the sagittal plane to match the flexion angle of the SAFER HBM.

3.2 FE modelling

3.2.1 Bone modelling

To be able to generate a good quality mesh, the scaled geometry models were meshed using the *Hexa Block* topology in ANSA. The geometry models were covered in manually placed hexahedral blocks to capture the shape of the surface. To capture the different properties of the bones, the cortical and the trabecular structures were modelled with separated Hexa Blocks. As described in Section 2.2.1 the cortical thickness varies along the femur, thus the thickness of the outer Hexa Blocks needs to vary accordingly.

The edges of the Hexa Blocks were projected onto the surface of the geometries. Internal Hexa Blocks, which represents the trabecular bone, were created using the *O-grid* function. The cortical bone were represented by one block over the thickness at the ends and two blocks over the thickness at the mid-shaft due to larger cortical thickness. The cortical thickness was applied in the anterior, posterior, lateral and medial directions at four cross-sections at the mid-shaft accordingly to normalized

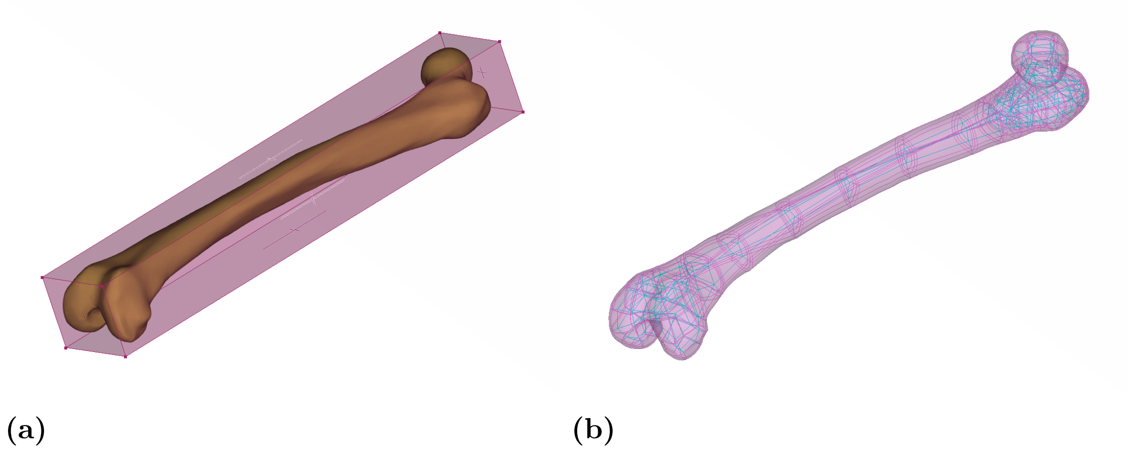

Figure 3.1: Illustration of Hexa Block generation **(a)** geometry model of the femur covered by one Hexa Block. **(b)** All generated Hexa Blocks to capture the shape of the femur.

values of [25]. The cortical thickness of the proximal end was applied in anterior, posterior, superior and inferior direction according to [23]. Due to limited information of the cortical thickness of the distal end, the thickness in all directions was set to 1.3 mm, according to [20]. The study conducted by Klein et al. [26] was used as a validation set, to compare the total and cortical cross-sectional areas.

In Figure 3.1 the generation of the Hexa Block topology is illustrated. In Figure 3.1a the geometry model of the femur is covered by one Hexa Block, which is not enough to capture the shape and the curvature of the femur. Instead, several blocks were used to capture the shape, as seen in Figure 3.1b. The purple blocks in the figure represent the cortical bone tissue, and the blue blocks the internal trabecular bone tissue.

The patella was covered with Hexa Blocks in similar fashion as the femur. The outer surface was first captured by Hexa Blocks, the internal were created with the O-grid functionality. The thickness of the outer blocks, the cortical Hexa Blocks, were defined as 4 mm according to [60].

The scaled femur and patella, covered with Hexa Blocks, were meshed according to the mesh quality criteria in [38]. All the generated elements must fulfil the 100% element quality limit, as stated in Table 2.1 for solid elements. The Hexa Blocks were meshed using fully integrated eight node solid elements.

The bone tissues were assumed to be of isotropic material behaviour, the properties defined in ANSA are tabulated in Table 3.1. Material card MAT24, **MAT PIECEWISE LINEAR PLASTICITY*, was used to describe the mechanical properties of the cortical bone tissue of the femur. Material card MAT1, **MAT ELASTIC*, was used to describe the mechanical properties of the trabecular bone tissue of the femur and the patella bone tissues.

3.2.2 Ligament and cartilage modelling

The four major ligaments, PT, QT and the cartilage on the distal femoral end, the tibia plateau and the posterior side of the patella were modelled based on descriptions from the literature, due to the lack of available geometry models. The existing mesh of the tibia from the SAFER HBM were kept in the knee model, hence the existing tibial plateau must be adjusted to the scaled geometry model. Else, the proportions between the distal femoral end and the tibial plateau will be lost. One way to adjust the existing mesh is to use the *Morphing topology*. Morphing is a module which allows modification to a mesh accordingly to a new design without change of node ID or element ID. The upper part of the SAFER HBM's tibia was morphed accordingly to the scaled and rotated geometry model. Hence, the existing mesh was adjusted to match the proportions of the scaled geometry.

A four-step methodology were used to model the ligaments and tendons. Firstly, the bone-ligaments insertion points were identified. Secondly, the geometrical cross-sections were defined. Thirdly, the cross-sections were swept between the insertion points along a spline, to create surface models. The spline were defined as close to the bone as possible to remove the risk of laxity. Lastly, the created surface models were covered manually with Hexa Blocks to generate the fully integrated eight node solid elements. The Hexa Block generation is visualized in Figure 3.2.

The insertion points of the collateral ligaments were identified accordingly to the description in sagittal plane by [33]. The cross-sections were defined as ellipses at the mid-distance between the insertion points. When generating the Hexa Blocks, the cross-section was not completely covered. The border ends that runs along the ligament were neglected to minimize the risk of warped and skewed elements.

The insertion points of the cruciate ligaments at the tibial plateau were identified according to [36]. Due to the limited information of the femoral insertion points, the insertion points were defined where the distance from the tibial insertion point was reasonable to the condyles according to [50]. The cross-sections were defined as circles at three levels, tibial and femoral insertion and at mid-length based on [34]–[36], [50]. Then Hexa Blocks were projected on the defined cross-sections to capture the geometrics. An internal Hexa Block was created, using the O-grid function, to improve the element quality of the surface elements.

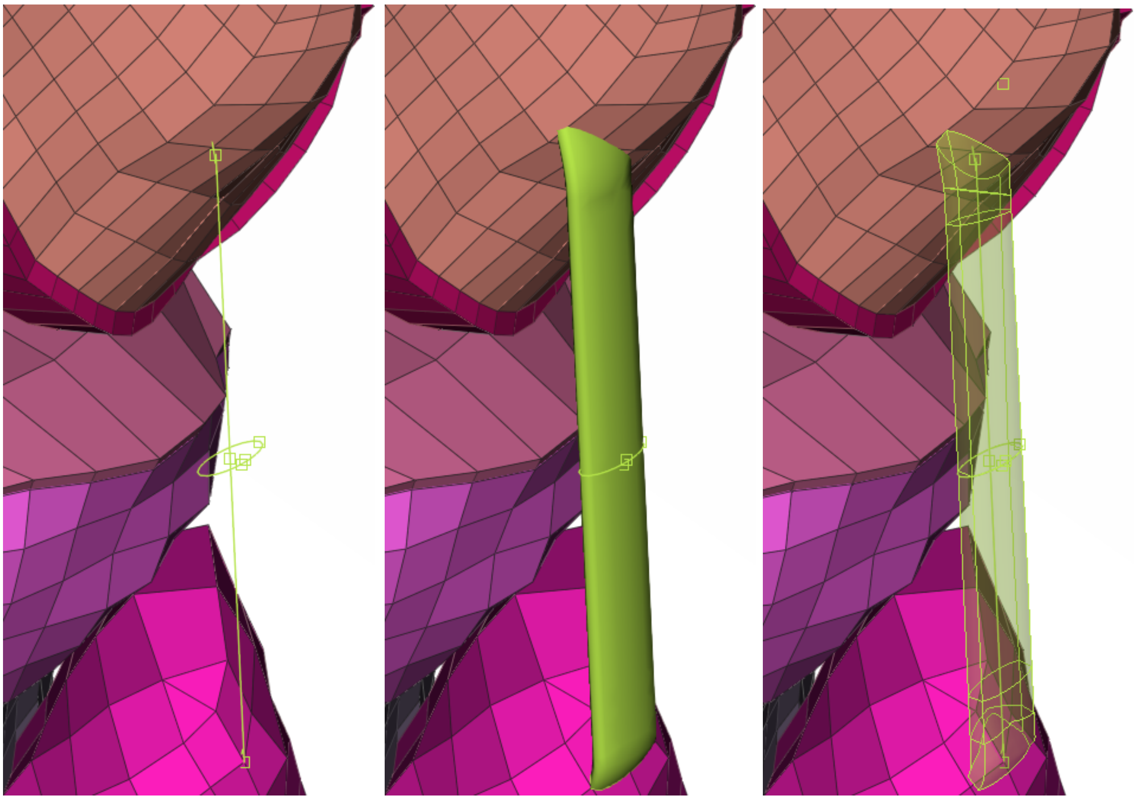

(a) **(b)** **(c)**

Figure 3.2: Illustration of Hexa Block generation of the LCL **(a)** Insertion points identified, defined cross-section and defined spline along the long axis of the LCL. **(b)** Generated a surface model by sweeping the cross-section along the spline. **(c)** All generated Hexa Blocks to capture the shape of the LCL.

The tibial insertion point of the patellar tendon was identified as the length of the PT according to [32], [61]. Due to the lack of information of the insertion to the patella, it was defined at the distal surface of the patella. The cross-section was defined as an ellipse with dimensions according to [61], at the mid-distance between the insertion points. Due to the elliptical cross-section of the PT, the border ends that runs along its length were not included in the Hexa Blocks, similar to the Hexa Blocks of the collateral ligaments described above.

The quadriceps tendon connects the patella to the quadriceps muscle. Since the SAFER HBM v10 is modelled without specific FE models of the muscles, the QT is assumed to connect to the femur, anteriorly. At mid-distance between the insertion points, the cross-section is defined as an ellipse. As for the previous elliptical ligaments, the Hexa Blocks does not cover the entire cross-section.

The cartilage covering the distal end of the femur, the tibial plateau and the posterior surface of the patella were modelled by extruding six or eight node solid elements from the cortical bone surface. Six or eight node solid elements, depending on the elements of the cortical bone tissue. The surface area to be extruded, and the thickness, were defined accordingly to the average male from Faber et al. [62].

Table 3.1: Mechanical properties defined in ANSA

Part	$\boldsymbol{E}$ [GPa]	$\boldsymbol{\rho}$ [kg/m^3]	$\boldsymbol{\nu}$ [-]	$\boldsymbol{\sigma_y}$ [MPa]	LS-DYNA Mat.	Ref.
Cortical[a]	19.9	2000	0.3	108	MAT24	[29]
Trabecular[a]	0.2	1000	0.3	-	MAT1	[27]
Cortical[b]	20	2000	0.3	-	MAT1	[27]
Trabecular[b]	1	1000	0.3	-	MAT1	[27]
ACL	0.123	1100	0.4	-	MAT1	[31]
PCL	0.168	1100	0.4	-	MAT1	[31]
MCL	0.224	1100	0.4	-	MAT1	[31]
LCL	0.280	1100	0.4	-	MAT1	[31]
QT	0.370	1100	0.4	-	MAT1	[31]
PT	0.336	1100	0.4	-	MAT1	[31]
Cartilage[c]	0.0252	1000	0.4	-	MAT1	

[a]Femur, [b]Patella, [c]Properties from the 50$^{\text{th}}$ percentile male SAFER HBM v10.

An exception was made on the tibial cartilage, the elements which were covered by the insertion areas of the cruciate ligaments were not covered by cartilage. Below the femoral condyles the femoral and tibial cartilage penetrated each other, hence the penetrated nodes of the tibial cartilage were translated to avoid penetration.

The material properties of the ligaments, tendons and cartilage are assumed to be linear isotropic, and are tabulated in Table 3.1. Material card MAT1, **MAT ELASTIC*, was used to define the properties of the modelled soft parts.

3.2.3 Contact modelling

When all parts were meshed, the contact between them were defined. Parts that shares nodes does not need to be considered, since they already are connected. The cortical and trabecular mesh share nodes, as well as the cartilage and respectively bone. The ligaments and the tendons were constrained to the bones. The nodes at the insertion areas of the ligaments were constrained to the bones by the contact definition of **CONTACT TIED NODES TO SURFACE*. This implies that selected nodes, at the end of each ligament or tendon, are tied to the surface segment of the bone.

To prevent penetration, including self penetration, of the modelled parts, the contact definition of **CONTACT AUTOMATIC SINGLE SURFACE* were defined, including all parts. This contact definition is sensitive to initial penetration, hence initial penetrations must be fixed before running a simulation.

3.3 Validation of femur model

3.3.1 FE modelling test setup

In total 23 male specimens were tested in three-point-bending and a combined loading of three-point-bending and axial compression [43]. This will be used as a validation set. The details of the tests and anthropometrics of the PMHS are tabulated in Appendix 1 A.2

The test setup have been used in previous validations of FE models of female femurs [13]. Thanks to in-house collaboration, the FE model of the test setup was carried over from the VIVA+ project. The imported test setup was improved to adjust the simulation to the potted external length (PEL), the length between the two rotations axis, which varied between the specimens as tabulated in Table A.8 and were adjusted for each simulation.

When using the imported test set up and the current modelled femur, the foam piece penetrated both the femur and the impactor. Therefore, two layers of 1 mm belytschko-tsay shell elements were generated as *MAT NULL SHELLS* on the top and bottom of the foam piece, to resolve the problem of penetration. The remodelled test setup used in the validation of the femur is displayed in Figure 3.3

All the parts, except the foam piece, in the setup were modelled as rigid materials with corresponding material properties. The potting cups, 6. in the figure, of PMMA were defined with E = 3.1 GPa, $\nu = 0.3$ and ρ = 1180 kg/m^3. The rigid parts were defined as aluminium with E = 70 GPa, $\nu = 0.34$ and ρ = 2700 kg/m^3. The material of the foam piece were defined as MAT57 *(*MAT LOW DENSITY FOAM)* material with a nominal stress versus strain curve extracted from [43] and ρ = 15.6 kg/m^3.

The ends of the femur were excluded and the long axis of the bone were aligned with the line connecting the centre of rotation of the potting cups. Each potting cup-holder, with linear bearings, were modelled as a revolute joint, which only allowed rotation around the Y-axis. The right cup, cup-holder and linear bearing in the figure were allowed to translate in X-direction, other degrees of freedom were restricted. Each of the 23 tests were modelled with associated prescribed displacement, as seen in Figure 3.4 for Test 1.01. The data in the figures were extracted from each individual test specimen using *WebPlotDigitizer, version 4.3.*

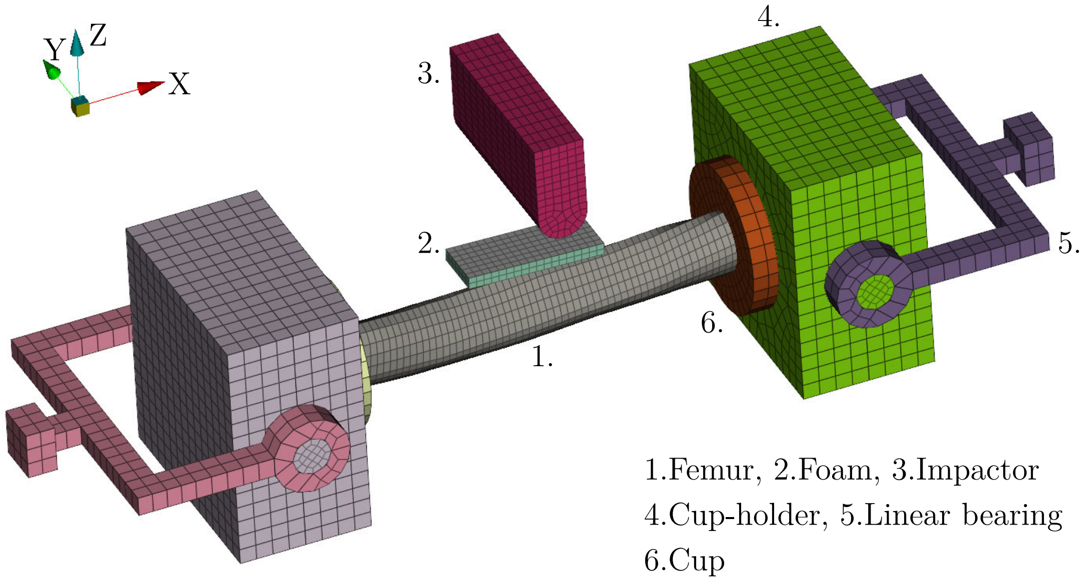

Figure 3.3: Isometric view of the three-point-bending test setup, imported and adjusted FE model from [13].

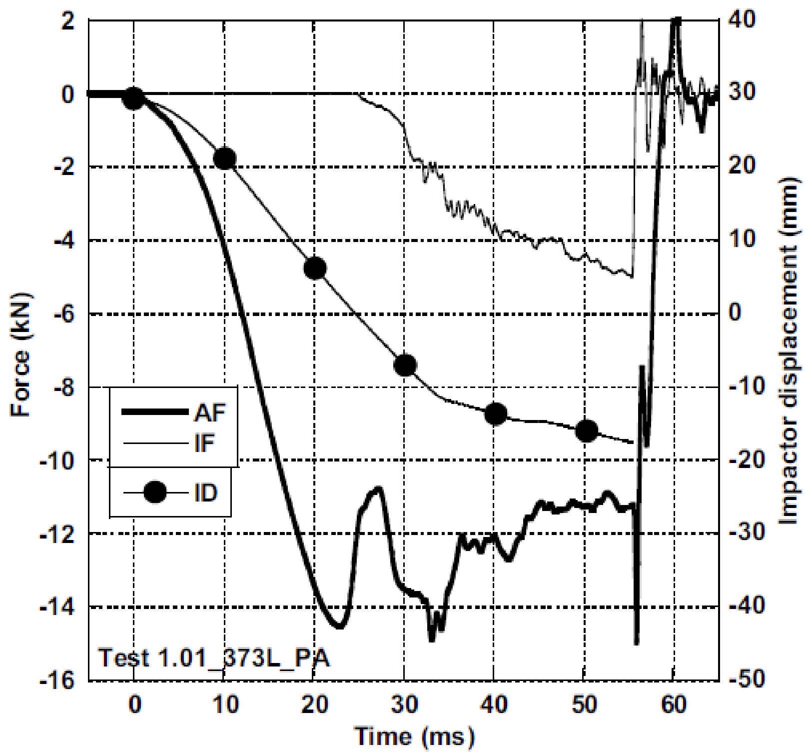

Figure 3.4: Example curve of combine load case extracted from [43]. AF- Axial Force, IF- Impactor Force and ID- Impactor Displacement. The scale of the ID is adjusted such that 0 corresponds to contact between the impactor and the foam. Reproduced by permission of the Stapp Association.

3.3.2 Post-processing

3.3.2.1 Statistical test corridors

The time-history results of the tests, time-displacement and time-force, in [43] were extracted using WebPlotDigitizer, and imported into MATLAB, (The Mathworks, Natick, MA). Data points before impact, impactor displacements before 0 mm, were excluded, hence no contact between the impactor and the foam piece are not of interest. There were five observed sets, one three-point-bending and four combined sets with different max axial load; 4,8,12,16 kN. The impactor force were interpolated from zero to the point where minimum displacement occurred within the observed set, by use of the inbuilt MATLAB function *interp1.m*. Then the standard deviation in each displacement step was computed by use of the inbuilt MATLAB function *std.m*, which is based on the sample standard deviation described in (2.8). Lastly, the corridors of $\pm 2SD$ of each observed set were plotted together with the result of the simulations.

3.3.2.2 CORA

The CORA evaluation was made in the CORA software *CORA 3.6.1*, (PDB, Gaimersheim, Germany). As in the previous method, the time-history results were used as correlation reference. The start time of the evaluation was set to the time step where the impactor impacted the bone, i.e. where the displacement was below zero. The end time of the evaluation was identified as 95% of the time from the first data point after impact to the last data point in the time-displacement test data. The last 5% were neglected since the models can not predict fracture, thus it can not capture the suddenly reduced load capability of the femur as seen in the test result.

The time-displacement data of the simulation were adjusted to account for the initial displacement of the impactor in the tests. The initial displacement of the impactor was added to the displacement data of the simulations.

Once the time-history data were extracted, it was imported into CORA. Both the cross-correlation and the corridor method were used when evaluating the curve to curve comparison. The parameters in CORA were set to default values according to the CORA manual [59].

The two methods, corridor and cross-correlation, and a combination of them two were computed for all the time-displacement and the time-force data. The time-displacement were analysed using CORA to evaluate if the input off the impactor displacement were correctly defined for the simulations.

4

Results

In this chapter, major results using the methods described in the previous chapter will be presented.

4.1 FE models

In total 28499 eight node solid elements and 4 six node solid elements were generated to model the body parts. The developed models are visualized in Figure 4.1. The femur was modelled with 25171 eight node solid elements with an average element side length of 2.94 mm.

In Figure 4.2 the element quality, described in Section 2.3.1, are visualized using bar plots. In Appendix 1 A.1 the details of the element quality measures are tabulated.

To reach the time step described in Section 2.3.1 the mass of the developed models including the tibia and the fibula are scaled with 5.26% from 1.52 kg to 1.60 kg.

4.2 Cortical thickness

In Figure 4.3 the cortical thickness distribution of the femur is displayed as a fringe plot. The cortical thickness in the figure is the average thickness computed at each corner node of the solid element. Where there are two layers of elements, the thickness is computed from the corner nodes of the outer face of the elements on the

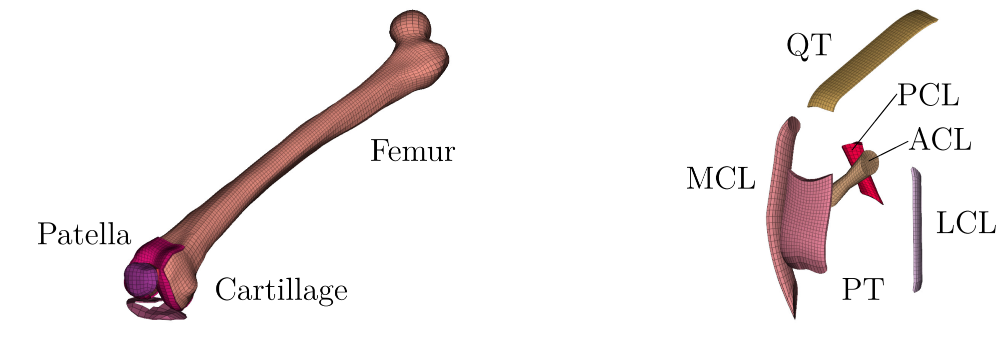

(a) **(b)**

Figure 4.1: Developed **(a)** bones with cartilage and **(b)** ligaments and tendons.

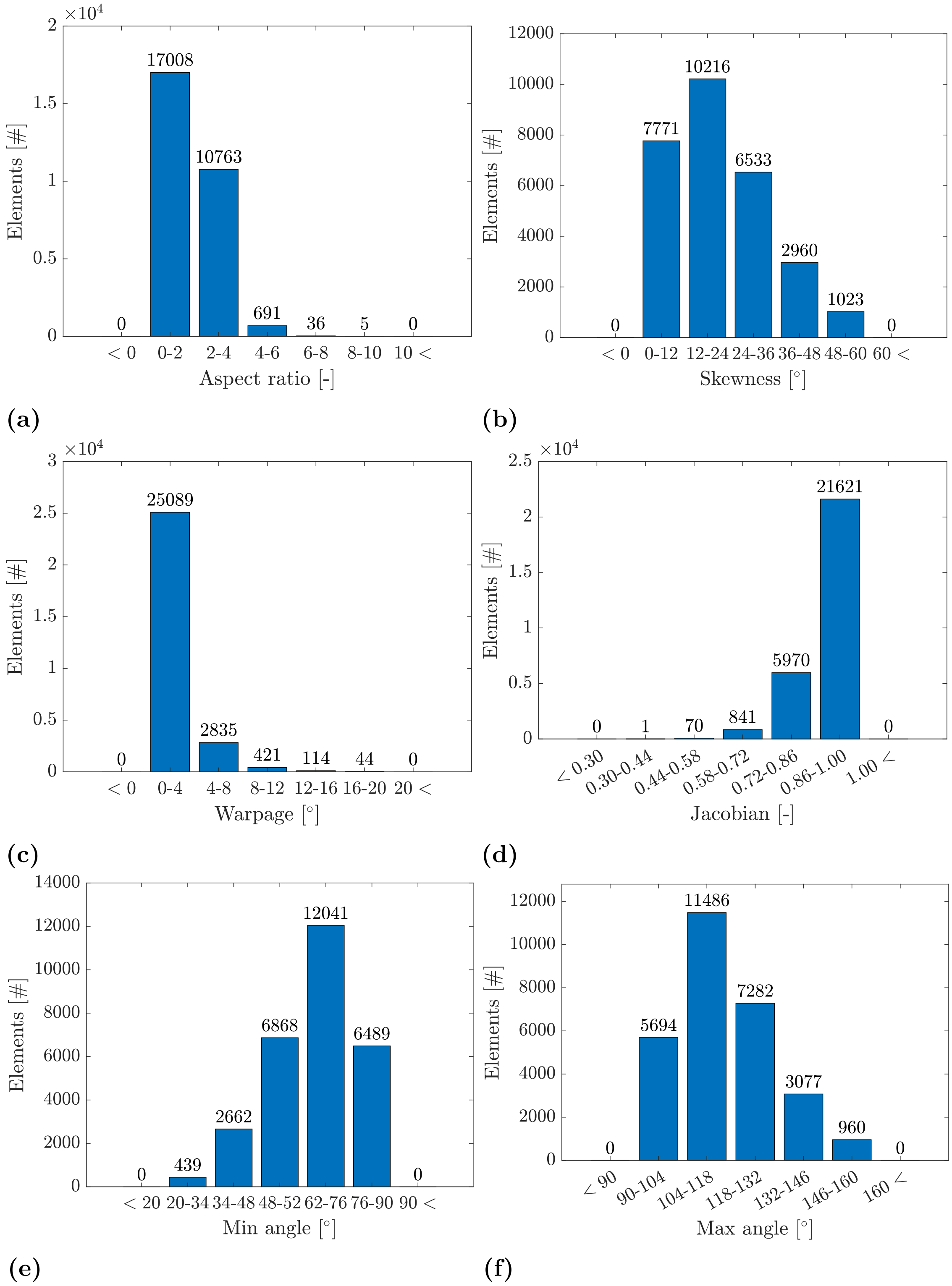

Figure 4.2: Bar plots of the element quality measures of all modelled elements described above: **(a)** Aspect ratio, **(b)** Skewness, **(c)** Warpage, **(d)** Jacobian, **(e)** Minimum Hexa angle and **(f)** Maximum Hexa angle.

outermost layer to the corner nodes of the inner face of the elements on the innermost layer. The thickness was computed using *S.GRAPH* in ANSA. The cortical thickness grows from the distal and proximal ends toward the mid-shaft, where the maximum cortical thickness occurs posteriorly.

In Table 4.1 a comparison to [26] is tabulated at six sections of the femur. The data from [26] is presented as mean, minimum and maximum values and the data from the model is measured in ANSA at each defined section.

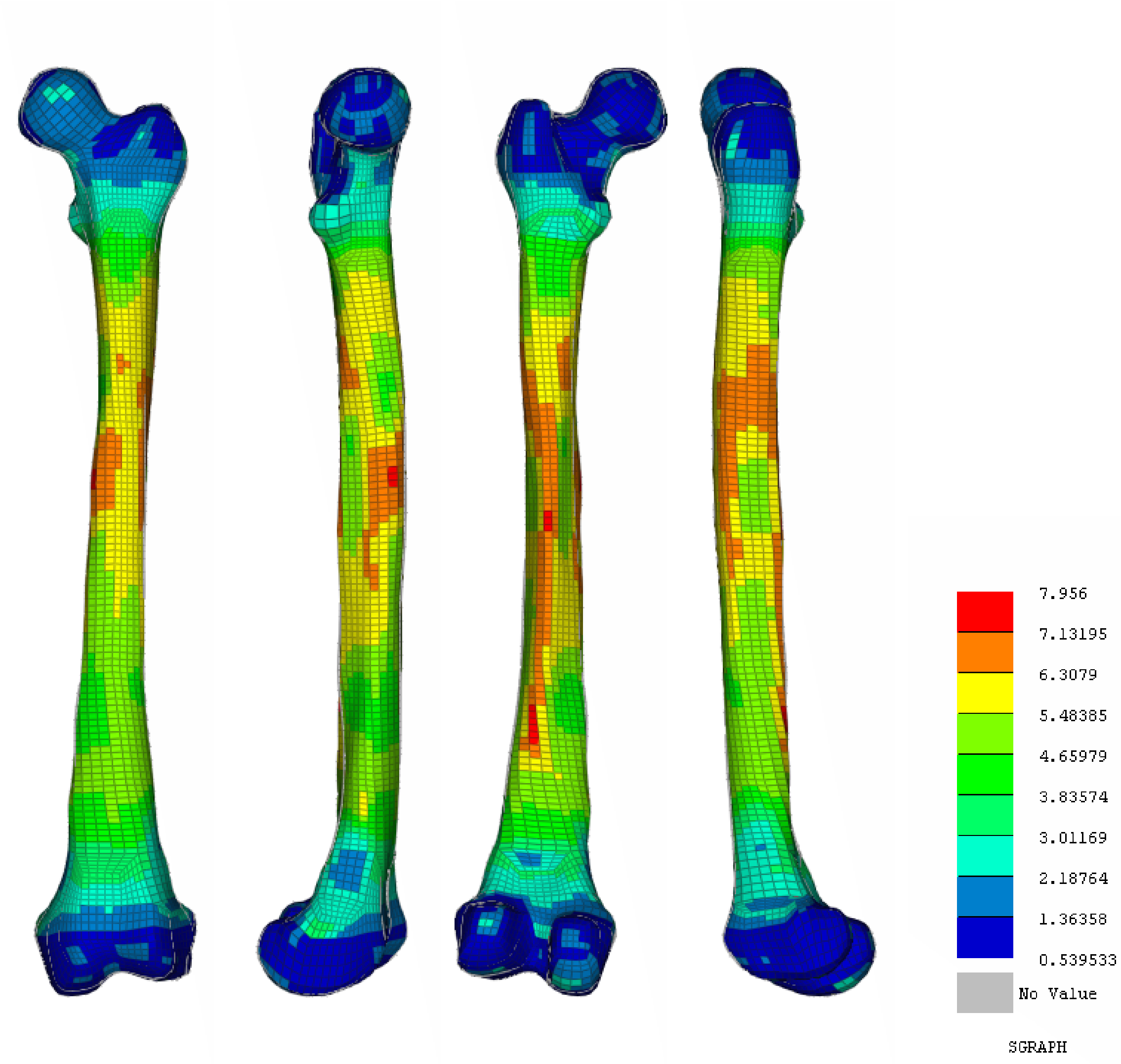

(a) **(b)** **(c)** **(d)** **(e)**

Figure 4.3: Cortical thickness distribution of the femur displayed in **(a)** anterior, **(b)** medial, **(c)** posterior and **(d)** lateral view and **(e)** scale in mm.

Table 4.1: Comparison on cross-sectional areas between Klein et al. [26] and femur model.

Section		**Klein et al. [26]**		**Model**	
		Total [mm^2]	Cortical [mm^2]	Total [mm^2]	Cortical [mm^2]
	min	604	-		
Neck	mean	783	-	847	-
	max	891	-		
	min	667	489		
1	mean	741	533	814	482
	max	804	587		
	min	574	432		
2	mean	648	509	684	468
	max	724	563		
	min	585	427		
3	mean	637	476	675	465
	max	698	524		
	min	622	390		
4	mean	674	449	688	428
	max	730	487		
	min	707	314		
5	mean	828	365	906	499
	max	898	422		

4.3 Validation of femur model

In Figure 4.4a two typical load curves, one three-point-bending and one combined load case, of the impactor displacement versus the reaction force obtained by the simulations are displayed and compared to the test data. The remaining 21 load curves are displayed in Figures A.1-A.5 in Appendix 1 A.3.

4.3.1 Statistical corridors

In Figure 4.5 the reaction force versus impactor displacement are plotted for the three-point-bending set and the four combined load sets with statistical computed corridors as described previous.

The solid curves in the figure represent the statistical computations, the mean and ± 2 standard deviations of the test results from [43], and the dashed curves corresponds to each simulation within the set. Note that the displacement are plotted from 0 to minimum displacement within the respective test set.

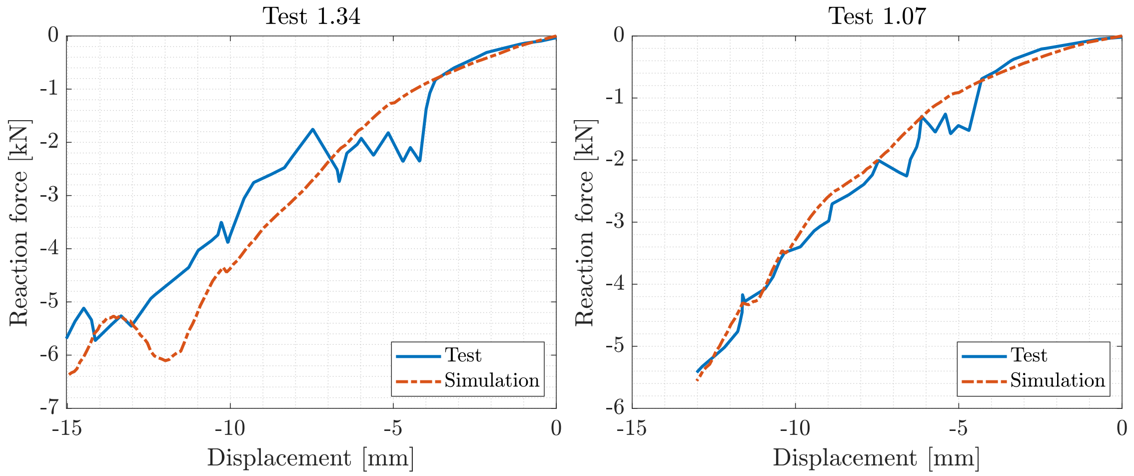

(a) **(b)**

Figure 4.4: Example load curves for **(a)** three-point-bending, test 1.34, and **(b)** combined loading of three-point-bending and axial compression, test 1.07.

4.3.2 CORA

In Tables 4.2 and 4.3 the result of the CORA time-force evaluation for the three-point-bending set and the combined set are tabulated. In Appendix 1 A.4 the complete CORA evaluation are tabulated and the time-force comparison curves are visualized within the comparison interval.

The most interesting result of the CORA evaluation in a validation point of view is the time-force comparison, it ranks and indicates which comparisons correlate more than others. The averaged combined result of the two loading cases was 0.720 for the three point bending set and 0.752 for the combined loading set. Thus, the simulations of the combined loading set showed greater correlation to its reference than the simulations of the three-point-bending set.

Table 4.2: CORA time-force evaluation three-point-bending

Test	Corridor	Cross-Correlation	Combined
1.34	0.766	0.913	0.840
1.37	0.487	0.586	0.536
1.38	0.482	0.752	0.617
2.06	0.831	0.850	0.840
2.07b	0.660	0.878	0.769
Average:	**0.645**	**0.796**	**0.720**

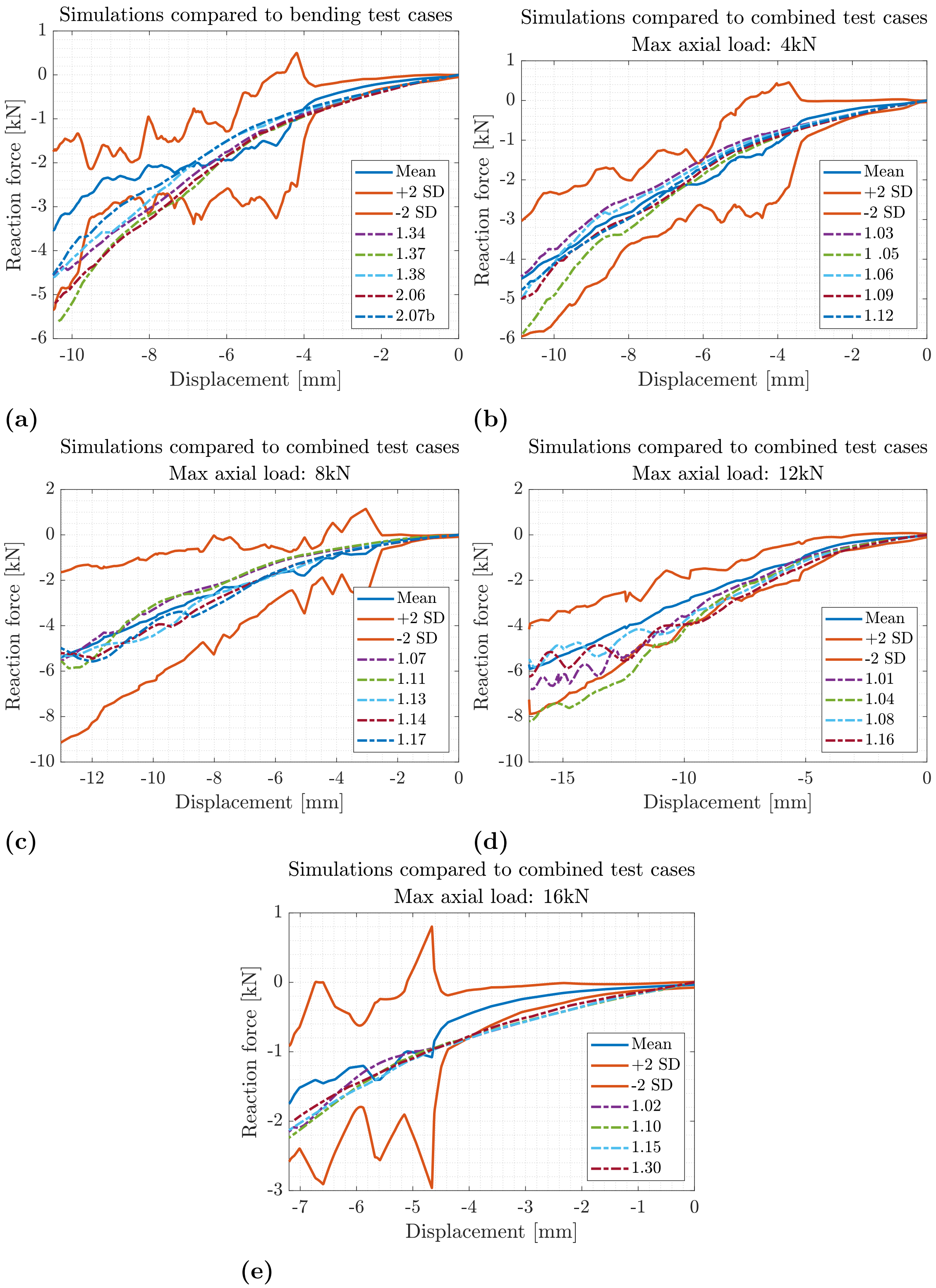

Figure 4.5: Corridors for **(a)** three-point-bending, **(b)** combined loading with max axial compression load of 4 kN,**(c)** combined loading with max axial compression load of 8 kN,**(b)** combined loading with max axial compression load of 12 kN and **(e)** combined loading with max axial compression load of 16 kN.

Table 4.3: CORA time-force evaluation combined loading

Test	Corridor	Cross-Correlation	Combined
1.01	0.245	0.807	0.526
1.02	0.424	0.611	0.575
1.03	0.724	0.790	0.757
1.04	0.678	0.911	0.794
1.05	0.773	0.812	0.792
1.06	0.878	0.938	0.908
1.07	0.950	0.963	0.956
1.08	0.833	0.818	0.826
1.09	0.849	0.750	0.799
1.10	0.588	0.895	0.741
1.11	0.815	0.909	0.862
1.12	0.741	0.786	0.763
1.13	0.490	0.836	0.663
1.14	0.578	0.785	0.681
1.15	0.231	0.805	0.518
1.16	0.936	0.962	0.949
1.17	0.837	0.881	0.859
1.30	0.645	0.478	0.562
Average:	**0.679**	**0.819**	**0.752**

5 Discussion

The aim of this thesis was to model and validate a knee-femur model for the 50$^{\text{th}}$ percentile male SAFER HBM. Due to available resources, the femur was based on a CT-scan of an average female and then scaled accordingly to the existing femur of the 50$^{\text{th}}$ percentile male SAFER HBM v10. To be able to capture the average male with all variations of the male population, a different method could have been used. E.g. the CT-scan could have been of an average male, or based on an average male computed CT-scans from a large set of males.

The modelled ligaments, tendons and cartilage are based on geometrical data from publications. Therefore, the size and the shape had to be simplified. E.g. the irregular cross-sectional shape of the cruciate ligaments was simplified to circular cross-sections. If medical images were available, the size and shape could have been captured more realistic and more accurate.

In Table 4.1 the modelled femur is compared to a statistical analysis made by Klein et al. based on femurs from 62 males with ages ranging from 18-89 years [26]. The total cross-sectional area in four sections of the modelled femur lays within the range min-max range of the study. Whereas in the other sections, the cross-sectional areas are greater than the maximum of the range. In three of the sections, the cortical cross-sectional areas are within the min-max range of the study. Whereas, the cortical cross-sectional area of one section is below the minimum of the range and the cortical area of one section is above the maximum of the range. The intention of the comparison with the study of Klein et al. was to evaluate geometrical properties in an unbiased way with a new set of properties. In four of the sections, the model correlates to Klein's study. The total cross-sectional area is related to the scaling of the geometry model, before meshing. Since the cross-sectional area of all sections are above the mean, the scaling factor in the transverse directions could have been decreased to properly fit the mean cross-sectional area of Klein et al.

The cortical cross-sectional area is related to the meshing procedure. The cortical thickness was applied in transverse direction along the femur. At four of the sections, the cortical cross-sectional area is below the mean value of the study. Since the stiffness of the femur is mainly related to the cortical bone layer, the geometrical contribution to the stiffness may be too low.

The average body mass and stature of the males used in the two validation load cases, three-point-bending and combined loading, by Ivarsson et al. were 87.0 kg and 183.9 cm, which are above the average male 78.2 kg and 175 cm established in the 1960s [2] and 77.3 kg 175.3 cm established in the 1980s [24]. Even if the anthropometrics are above average, the study conducted by Ivarsson et al. [43] was the only one found in the literature study which fulfilled the criteria of in-data to be used as validation set.

The average femur length, measured along the long axis of the shaft between the most proximal and distal point, of the 62 male specimens in Klein et al. study was 481 mm [26]. The length of the modelled femur, based on the existing femur in SAFER HBM v10, was 472 mm. However, the stature of the males used in [26] are not published. If the stature of the males corresponds to the average male, 175 cm, the modelled femur can be scaled 2% along the long axis of the femur.

Ivarsson et al. measured three parameters of the mid-shaft, lateral and sagittal diameter and the circumference [43]. The averaged lateral and sagittal diameter of the mid-shaft were 29 mm and 32 mm, respectively. The averaged mid-shaft circumference was 105 mm. The lateral diameter, sagittal diameter and circumference of the mid-shaft of the modelled femur were 27 mm, 34 mm and 97 mm, respectively. As mentioned above, the averaged PMHS used in [43] are larger than the 50^{th} percentile male. It is reasonable that the sagittal diameter and the circumference of the model are less than the average of the PMHS used in the test. However, the lateral diameter of the model is larger than the average lateral diameter of the PMHS. Since the total area of cross-section 3, compared to Klein were reasonable, the lateral diameter of the model is left unchanged and is assumed to compare reasonably to an average male.

In general, by ocular assessment of Figures A.1-A.5 the modelled femur appears to be stiffer than the specimen tested by Ivarsson et al. [43]. The simulated femur requires a greater force than the tested to displace the impactor the equal distance.

Two of the specimens exposed to combined loading, Test 1.12 and Test 1.13 visualized in Figure A.3, behaves differently than the rest. The tested specimens require a greater force than the simulated femur to achieve equal impactor displacement. The specimens from these tests belongs to the same PMHS, an obese 58-year-old male weighing 141.0 kg. 141.0 kg is almost twice the weight of the 50^{th} percentile male. According to Wolff's law, the bone tissues adapt during growth, due to the various loads over time [27]. I.e. bone tissues which are exposed to greater loads will adapt to be able to withstand the increased load. Hence, the high weight of the PMHS can explain why the result of these specimens are significant different from the rest.

At the end of some simulations, the force-displacement curve starts to oscillate. One reason for this behaviour can be that the impactor induces motions close to the natural frequencies of the femur, hence the femur starts to oscillate, see e.g. Test 1.10 in Figure A.2. When the femur oscillates away from the impactor, the contact between the foam and bone is reduced, thus also the reaction force.

By ocular assessment of Figure 4.5 the simulations capture the response of the femur in an adequate way. For the four sets of combined loading, the majority of the simulations stays within the corridors. The set of three-point-bending, Figure 4.5a, indicates that the simulated femur appears to be stiffer than the mean of the tests. At a displacement of -7 to -10 mm, the simulated femur is exposed to greater force than the tests. This behaviour is not dominant for the combined load cases. Where the simulations and the mean of the tests showed a greater correlation.

The intention of curve-to-curve compare the simulations and tests conducted by Ivarsson et al. [43] was to quantify the correlation in an objective way. All results of the CORA evaluation are tabulated in Table A.9 in Appendix 1 A.4 for the three-point-bending tests and the combined load case, respectively. The averaged combined result, CD, of the two methods of the time-displacement data were 0.994 for the three-point-bending set and 0.995 for the combined load case. These results are close to perfect correlation, which indicates that the prescribed motion were correctly extracted from Ivarsson et al. [43].

The averaged CD of the time-force was 0.720 for the three-point-bending set and 0.752 for the combine load set. This indicates that the combined load set shows a greater correlation than the three-point-bending set. But both sets show a good correlation between the simulations and the tests.

5.1 Future work

Before the knee model is integrated in a SAFER HBM, it must be completely validated. The ligaments, tendons and the complete knee model must be validated in a kinematic sense to ensure the biofidelity of the model. In this project, only the femur has been validated, and the modelled soft tissues must be validated in the future.

To achieve biofidelity of the modelled soft tissues, the material models need to be updated. In this project, the modelled ligaments, tendons and cartilage have been modelled with linear elastic models. The material models must be updated to a hyperelastic material model with limits to restrict the models to definite stress or strains to a similar to the typical load-strain curve displayed in Figure 2.3. And even more favourable to a visco-hyperelastic material model to compensate for the loading rate.

The future intention of the model is to be able to make injury assessment to the modelled parts. Before the model can be used for injury assessment, resources must be put into relating local strain or stress measures to the risk of injury in order to create injury risk functions.

5.2 Limitations

To be able to carry out this project in time and to satisfy the demands of a Master's thesis, several limitations were made at the beginning of the thesis:

- The model will be based on a 50^{th} percentile male, i.e. average male. Hence, THUMS v3 is based on a 50^{th} percentile male, thus also SAFER HBM v10. Morphing procedures can be used to capture the remaining parts of a population.
- A denuded knee and femur will be modelled, i.e. skin, fat and muscle-tissues will not be modelled. Hence, the tissues and its properties will be a carry over from previous SAFER HBMs and morphed to fit the model.
- The model and its sub-parts will be validated in a kinetic and kinematic sense, e.g. validated using known load-path curves from known experiments.

6
Conclusion

High resolution FE models of the knee and femur, with connecting soft tissues: ligaments and tendons, were developed. The femur was validated in two types of loading, three-point-bending and a combined loading of three-point-bending and axial compression. The validated femur can be integrated in a 50^{th} percentile male SAFER HBM and used to create injury risk functions.

The aim of validation of the knee have not been achieved. Preferably, one or several of the studies found in the literature study can be used as validation sets. One approach can be to first validate the knee with a four-point bending and then after integration in a 50^{th} percentile male SAFER HBM, a knee impact test can be used as validation of the lower extremity.

Bibliography

[1] *Global status report on road safety 2018*. Geneva: World Health Organization, 2018, vol. Licence: CC BY-NC-SA 3.0 IGO, ISBN: 978-92-4-156568-4.

[2] K.-U. Schmitt, P. F. Niederer, M. H. Muser, and F. Walz, *Trauma Biomechanics: Accidental Injury in Traffic and Sports*. Springer-Verlag Berlin Heidelberg, 2010, vol. Third edition, ISBN: 978-3-642-03712-2.

[3] C. Simms and D. Wood, *Pedestrian and Cyclist Impact: A Biomechanical Perspective*. Springer, Dordrecht, 2009, vol. First edition, pp. 5–30, ISBN: 978-90-481-2742-9.

[4] *Persons hospitalized due to road traffic accidents 2014*, Jun. 2016. [Online]. Available: `https://www.trafa.se/vagtrafik/vagtrafikskadade-inom-sjukvarden/`.

[5] A. Mallory, R. Fredriksson, E. Rosén, and B. Donnelly, "Pedestrian injuries by source: Serious and disabling injuries in us and european cases," *Annals of advances in automotive medicine. Association for the Advancement of Automotive Medicine. Annual Scientific Conference*, vol. 56, pp. 13–24, 2012.

[6] J. Saadé, S. Cuny, M. Labrousse, E. Song, C. Chauvel, and P. Chrétien, "Pedestrian injuries and vehicles-related risk factors in car-to-pedestrian frontal collisions," in *Proceedings of the 2020 IRCOBI Conference Proceedings*, 2020, pp. 278–289.

[7] K. D. Klinich, "Biomechanics of pedestrian injuries related to lower extremity injury assessment tools: A review of the literature and analysis of pedestrian crash database," 2003.

[8] N. Ottosen and H. Petersson, *Introduction to the Finite Element Method*. Prentice Hall, 1992, ISBN: 978-0-13-473877-2.

[9] M. Iwamoto, Y. Kisanuki, I. Watanabe, K. Furusu, K. Miki, and J. Hasegawa, "Development of a finite element model of the total human model for safety (thums) and application to injury reconstruction," in *Proceedings of the international IRCOBI Conference*, 2002, pp. 18–20.

[10] K. Shigeta, Y. Kitagawa, and T. Yasuki, "Development of next generation human fe model capable of organ injury prediction," *Proceedings of the 21st Annual Enhanced Safety of Vehicles*, pp. 15–18, 2009.

[11] F. S. Gayzik, D. P. Moreno, N. A. Vavalle, A. C. Rhyne, and J. D. Stitzel, "Development of a full human body finite element model for blunt injury prediction utilizing a multi-modality medical imaging protocol," in *12th International LS-DYNA User Conference*, 2012, pp. 3–5.

[12] M. L. Davis, B. Koya, J. D. Stitzel, and F. S. Gayzik, "Development of the ghbmc 5th percentile female finite element model," in *2015 Ohio State University Injury Biomechanics Symposium*, 2015.

[13] A. Schubert, N. Erlinger, C. Leo, J. Iraeus, J. John, and C. Klug, "Development of a 50th percentile female femur model," *Proceedings of the IRCOBI Conference*, 2021.

[14] R. L. Drake, A. W. Vogl, and A. W. Mitchell, *GRAY'S ANATOMY FOR STUDENTS*. Elisver Inc., 2020, vol. 4th Edition, ISBN: 978-0-323-39304-1.

[15] *Anatomy and physiology*, 2013. [Online]. Available: `https://openstax.org/details/books/anatomy-and-physiology`.

[16] H. J. Woodhead, A. F. Kemp, C. J. Blimkie, *et al.*, "Measurement of mid-femoral shaft geometry: Repeatability and accuracy using magnetic resonance imaging and dual-energy x-ray absorptiometry," *Journal of Bone and Mineral Research*, vol. 16, no. 12, pp. 2251–2259, 2001.

[17] D. M. Cooper, C. D. L. Thomas, J. G. Clement, A. L. Turinsky, C. W. Sensen, and B. Hallgrímsson, "Age-dependent change in the 3d structure of cortical porosity at the human femoral midshaft," *Bone*, vol. 40, no. 4, pp. 957–965, 2007.

[18] T. J. Beck, A. C. Looker, C. B. Ruff, H. Sievanen, and H. W. Wahner, "Structural trends in the aging femoral neck and proximal shaft: Analysis of the third national health and nutrition examination survey dual-energy x-ray absorptiometry data," *Journal of Bone and Mineral Research*, vol. 15, no. 12, pp. 2297–2304, 2000.

[19] P. Zioupos and J. Currey, "Changes in the stiffness, strength, and toughness of human cortical bone with age," *Bone*, vol. 22, no. 1, pp. 57–66, 1998.

[20] W. Du, J. Zhang, and J. Hu, "A method to determine cortical bone thickness of human femur and tibia using clinical ct scans," in *2018 IRCOBI conference proceedings, Athens (Greece)*, 2018, pp. 403–412.

[21] S. Feik, C. Thomas, R. Bruns, and J. Clement, "Regional variations in cortical modeling in the femoral mid-shaft: Sex and age differences," *American Journal of Physical Anthropology*, vol. 112, no. 2, pp. 191–205, 2000.

[22] F. Gaillard, *Femur (illustration)*, 2009. [Online]. Available: `https://radiopaedia.org/cases/7555`.

[23] M. Malo, D. Rohrbach, H. Isaksson, *et al.*, "Longitudinal elastic properties and porosity of cortical bone tissue vary with age in human proximal femur," *Bone*, vol. 53, no. 2, pp. 451–458, 2013, ISSN: 8756-3282.

[24] L. W. Schneider, "Development of anthropometrically based design specifications for an advanced adult anthropomorphic dummy family, volume 1. final report," Tech. Rep., 1983.

[25] K. Someya, T. Mochizuki, S. Hokari, *et al.*, "Age- and sex-related characteristics in cortical thickness of femoral diaphysis for young and elderly subjects," *Journal of Bone and Mineral Metabolism*, vol. 38, no. 4, pp. 533–543, 2020, ISSN: 1435-5604.

[26] K. F. Klein, J. Hu, M. P. Reed, C. N. Hoff, and J. D. Rupp, "Development and Validation of Statistical Models of Femur Geometry for Use with Parametric

Finite Element Models," *Ann Biomed Eng*, vol. 43, no. 10, pp. 2503–2514, 2015.

[27] R. B. Martin, D. B. Burr, N. A. Sharkey, and D. p. Fyhrie, *Skeletal Tissue Mechanics*. Springer, 2015, vol. Second Edition, ISBN: 978-1-4939-3002-9.

[28] S. C. Cowin and S. B. Doty, *Tissue Mechanics*. Springer Science+Business Media, LLC, 2007, ISBN: 978-0-387-36825-2.

[29] H. H. Bayraktar, E. F. Morgan, G. L. Niebur, G. E. Morris, E. K. Wong, and T. M. Keaveny, "Comparison of the elastic and yield properties of human femoral trabecular and cortical bone tissue," *J Biomech*, vol. 37, no. 1, pp. 27–35, 2004.

[30] P. K. Zysset, X. E. Guo, C. E. Hoffler, K. E. Moore, and S. A. Goldstein, "Elastic modulus and hardness of cortical and trabecular bone lamellae measured by nanoindentation in the human femur," *J Biomech*, vol. 32, no. 10, pp. 1005–1012, 1999.

[31] G. A. Orozco, P. Tanska, M. E. Mononen, K. S. Halonen, and R. K. Korhonen, "The effect of constitutive representations and structural constituents of ligaments on knee joint mechanics," *Sci Rep*, vol. 8, no. 1, p. 2323, 2018.

[32] C. Belvedere, A. Ensini, A. Feliciangeli, *et al.*, "Geometrical changes of knee ligaments and patellar tendon during passive flexion," *J Biomech*, vol. 45, no. 11, pp. 1886–1892, 2012.

[33] N. Otake, H. Chen, X. Yao, and S. Shoumura, "Morphologic study of the lateral and medial collateral ligaments of the human knee," *Okajimas Folia Anat Jpn*, vol. 83, no. 4, pp. 115–122, 2007.

[34] C. D. Harner, G. A. Livesay, S. Kashiwaguchi, H. Fujie, N. Y. Choi, and S. L. Woo, "Comparative study of the size and shape of human anterior and posterior cruciate ligaments," *J Orthop Res*, vol. 13, no. 3, pp. 429–434, 1995.

[35] C. D. Harner, G. H. Baek, T. M. Vogrin, G. J. Carlin, S. Kashiwaguchi, and S. L. Woo, "Quantitative analysis of human cruciate ligament insertions," *Arthroscopy*, vol. 15, no. 7, pp. 741–749, 1999.

[36] L. Zheng, C. D. Harner, and X. Zhang, "The morphometry of soft tissue insertions on the tibial plateau: data acquisition and statistical shape analysis," *PLoS One*, vol. 9, no. 5, e96515, 2014.

[37] J. o. Hallquist, *LS-DYNA® Theory manual*. Livermore Software Technology Corporation, 2006, ISBN: 0-9778540-0-0.

[38] B. Pipkorn, J. Östh, E. Brynskog, *et al.*, "Validation of the safer human body model kinematics in far-side impacts," in *Proceedings of the IRCOBI Conference*, 2021.

[39] J. R. Funk, J. R. Kerrigan, and J. R. Crandall, "Dynamic bending tolerance and elastic-plastic material properties of the human femur," *Annual proceedings. Association for the Advancement of Automotive Medicine*, vol. 48, pp. 215–233, 2004.

[40] J. R. Kerrigan, K. S. Bhalla, N. J. Madeley, J. R. Funk, D. Bose, and J. R. Crandall, "Experiments for establishing pedestrian-impact lower limb injury criteria," in *SAE 2003 World Congress & Exhibition*, SAE International, Mar. 2003. DOI: `https://doi.org/10.4271/2003-01-0895`.

[41] J. L. Forman, E. de Dios, I. Symeonidis, *et al.*, “Fracture tolerance related to skeletal development and aging throughout life: 3-point bending of human femurs,” in *IRCOBI Conference Proceedings, Dublin, Ireland*, 2012, pp. 529–539.

[42] E. A. Kennedy, W. J. Hurst, J. D. Stitzel, *et al.*, “Lateral and posterior dynamic bending of the mid-shaft femur: fracture risk curves for the adult population,” *Stapp Car Crash J*, vol. 48, pp. 27–51, 2004.

[43] B. J. Ivarsson, D. Genovese, J. R. Crandall, J. R. Bolton, C. D. Untaroiu, and D. Bose, “The tolerance of the femoral shaft in combined axial compression and bending loading,” *Stapp Car Crash J*, vol. 53, pp. 251–290, 2009.

[44] J. H. Keyak, S. A. Rossi, K. A. Jones, and H. B. Skinner, “Prediction of femoral fracture load using automated finite element modeling,” *Journal of Biomechanics*, vol. 31, no. 2, pp. 125–133, 1997, ISSN: 0021-9290. DOI: `https://doi.org/10.1016/S0021-9290(97)00123-1`. [Online]. Available: `https://www.sciencedirect.com/science/article/pii/S0021929097001231`.

[45] D. D. Cody, G. J. Gross, F. J. Hou, H. J. Spencer, S. A. Goldstein, and D. P. Fyhrie, “Femoral strength is better predicted by finite element models than qct and dxa,” *Journal of Biomechanics*, vol. 32, no. 10, pp. 1013–1020, 1999, ISSN: 0021-9290.

[46] M. Bessho, I. Ohnishi, J. Matsuyama, T. Matsumoto, K. Imai, and K. Nakamura, “Prediction of strength and strain of the proximal femur by a ct-based finite element method,” *Journal of Biomechanics*, vol. 40, no. 8, pp. 1745–1753, 2007, ISSN: 0021-9290.

[47] J. A. Van Dommelen, B. Ivarsson, M. M. Jolandan, *et al.*, “Characterization of the rate-dependent mechanical properties and failure of human knee ligaments,” *SAE transactions*, pp. 80–90, 2005.

[48] R. S. Jones, N. S. Nawana, M. J. Pearcy, *et al.*, “Mechanical properties of the human anterior cruciate ligament,” *Clinical biomechanics*, vol. 10, no. 7, pp. 339–344, 1995.

[49] S. L.-Y. Woo, J. M. Hollis, D. J. Adams, R. M. Lyon, and S. Takai, “Tensile properties of the human femur-anterior cruciate ligament-tibia complex: The effects of specimen age and orientation,” *The American journal of sports medicine*, vol. 19, no. 3, pp. 217–225, 1991.

[50] N. K. Paschos, D. Gartzonikas, N.-M. Barkoula, *et al.*, “Cadaveric study of anterior cruciate ligament failure patterns under uniaxial tension along the ligament,” *Arthroscopy: The Journal of Arthroscopic & Related Surgery*, vol. 26, no. 7, pp. 957–967, 2010.

[51] S. Balasubramanian, P. Beillas, A. Belwadi, W. N. Hardy, *et al.*, “Below knee impact responses using cadaveric specimens,” *Stapp Car Crash Journal*, vol. 48, p. 71, 2004.

[52] C. D. Harner, J. W. Xerogeanes, G. A. Livesay, *et al.*, “The human posterior cruciate ligament complex: An interdisciplinary study: Ligament morphology and biomechanical evaluation,” *The American journal of sports medicine*, vol. 23, no. 6, pp. 736–745, 1995.

[53] H.-J. Cho and D.-S. Kwak, "Mechanical properties and characteristics of the anterolateral and collateral ligaments of the knee," *Applied Sciences*, vol. 10, no. 18, p. 6266, 2020.

[54] J. Kerrigan, B. Ivarsson, D. Bose, *et al.*, "Rate-sensitive constitutive and failure properties of human collateral knee ligaments," in *Proc. IRCOBI Conf*, 2003, pp. 177–190.

[55] J. R. Robinson, A. M. Bull, and A. A. Amis, "Structural properties of the medial collateral ligament complex of the human knee," *Journal of biomechanics*, vol. 38, no. 5, pp. 1067–1074, 2005.

[56] J. D. Rupp, M. P. Reed, T. A. Jeffreys, and L. W. Schneider, "Effects of hip posture on the frontal impact tolerance of the human hip joint," *Stapp Car Crash J*, vol. 47, pp. 21–33, 2003.

[57] J. D. Rupp, C. S. Miller, M. P. Reed, N. H. Madura, K. D. Klinich, and L. W. Schneider, "Characterization of knee-thigh-hip response in frontal impacts using biomechanical testing and computational simulations," *Stapp Car Crash J*, vol. 52, pp. 421–474, 2008.

[58] D. Bose, K. Bhalla, L. Rooij, S. Millington, A. Studley, and J. Crandall, "Response of the knee joint to the pedestrian impact loading environment," in *2004 SAE World Congress*, 2004.

[59] C. Thunert, *CORA release 3.6 user's manual*, 2012. [Online]. Available: `https://www.pdb-org.com/en/`.

[60] T. Tanpowpong, T. Itthipanichpong, T. Huanmanop, N. Jaruthien, and N. Tangchitcharoen, "A cadaveric study of the location and morphology of the central patellar ridge for bone-patellar tendon-bone graft," *J Orthop Surg Res*, vol. 16, no. 1, p. 92, 2021.

[61] J. H. Yoo, S. R. Yi, and J. H. Kim, "The geometry of patella and patellar tendon measured on knee MRI," *Surg Radiol Anat*, vol. 29, no. 8, pp. 623–628, 2007.

[62] S. C. Faber, F. Eckstein, S. Lukasz, *et al.*, "Gender differences in knee joint cartilage thickness, volume and articular surface areas: assessment with quantitative three-dimensional MR imaging," *Skeletal Radiol*, vol. 30, no. 3, pp. 144–150, 2001.

A

Appendix 1

A.1 Element quality measures

All details of the element quality of the FE models are presented in Table A.1-A.7.

Table A.1: Element side length

		ALL[a]	**ACL**	**Cartilage**[a]	**Femur**	**LCL**	**MCL**	**Patella**	**PCL**	**PT**	**QT**
Min.	[mm]	0.33	0.52	0.40	0.54	0.68	0.84	0.62	0.33	0.86	0.66
Average	[mm]	2.86	1.35	3.64	2.94	1.83	2.92	3.98	1.60	2.34	1.77
Max.	[mm]	12.68	3.28	12.68	7.85	5.51	11.37	7.54	4.03	7.54	5.50

[a]Only considering eight node solid elements.

Table A.2: Skewness

		ALL	**ACL**	**Cartilage**	**Femur**	**LCL**	**MCL**	**Patella**	**PCL**	**PT**	**QT**
<0	[#]	0	0	0	0	0	0	0	0	0	0
0-12	[#]	7771	0	272	6750	88	64	56	15	198	328
12-24	[#]	10216	57	172	9317	40	133	130	161	164	42
24-36	[#]	6533	299	47	5900	10	14	76	145	32	10
36-48	[#]	2960	316	15	2429	7	13	35	131	14	0
48-60	[#]	1023	138	1	775	0	16	15	60	8	10
60<	[#]	0	0	0	0	0	0	0	0	0	0
Total	[#]	28503	810	507	25171	145	240	312	512	416	390
Min.	[°]	0.78	15.06	0.78	0.87	2.36	3.76	1.94	9.34	2.75	2.22
Average	[°]	21.3	37.87	13.31	21.09	12.03	19.48	23.10	31.63	14.72	8.02
Max.	[°]	59.99	59.98	50.97	59.99	40.90	59.95	53.63	59.69	55.36	59.97

Table A.3: Aspect ratio

		ALL	ACL	Cartilage	Femur	LCL	MCL	Patella	PCL	PT	QT
<0	[#]	0	0	0	0	0	0	0	0	0	0
0-2	[#]	17008	341	94	15342	113	51	190	364	137	376
2-4	[#]	10763	469	372	9149	32	187	113	148	279	14
4-6	[#]	691	0	9	671	0	2	9	0	0	0
6-8	[#]	36	0	27	9	0	0	0	0	0	0
8-10	[#]	5	0	5	0	0	0	0	0	0	0
>10	[#]	0	0	0	0	0	0	0	0	0	0
Total	[#]	28503	810	507	25171	145	240	312	512	416	390
Min.	[-]	1.00	1.13	1.52	1.00	1.11	1.49	1.11	1.03	1.01	1.03
Average	[-]	2.01	2.10	2.82	2.01	1.71	2.35	2.00	1.81	2.20	1.37
Max.	[-]	9.37	3.39	9.37	7.29	2.93	5.12	5.22	2.75	3.31	2.53

Table A.4: Warpage

		ALL	ACL	Cartilage	Femur	LCL	MCL	Patella	PCL	PT	QT
<0	[#]	0	0	0	0	0	0	0	0	0	0
0-4	[#]	25089	668	401	22420	133	204	96	411	383	373
4-8	[#]	2835	135	87	2354	12	13	148	64	18	4
8-12	[#]	421	5	14	298	0	13	49	25	11	6
12-16	[#]	114	2	2	71	0	8	15	10	4	2
16-20	[#]	44	0	3	28	0	2	4	2	0	5
>20	[#]	0	0	0	0	0	0	0	0	0	0
Total	[#]	28503	810	507	25171	145	240	312	512	416	390
Min.	[°]	0.01	0.48	0.12	0.06	0.05	0.12	1.00	0.42	0.04	0.01
Average	[°]	2.08	2.36	2.85	2.04	0.77	1.83	5.87	2.62	1.56	0.92
Max.	[°]	19.99	12.48	18.01	19.99	6.25	17.15	18.58	16.41	13.91	18.60

Table A.5: Jacobian

		ALL	ACL	Cartilage	Femur	LCL	MCL	Patella	PCL	PT	QT
<0.3	[#]	0	0	0	0	0	0	0	0	0	0
0.3-0.44	[#]	1	0	0	1	0	0	0	0	0	0
0.44-0.58	[#]	70	2	0	21	2	11	22	5	6	1
0.58-0.72	[#]	841	130	4	442	3	33	91	106	20	12
0.72-0.86	[#]	5970	195	22	5285	41	46	143	147	56	35
0.86-1.00	[#]	21621	483	481	19422	99	150	56	254	334	342
>1.00	[#]	0	0	0	0	0	0	0	0	0	0
Total	[#]	28503	810	507	25171	145	240	312	512	416	390
Min.	[-]	0.43	0.57	0.6	0.43	0.53	0.52	0.49	0.47	0.52	0.57
Average	[-]	0.89	0.85	0.92	0.89	0.9	0.85	0.75	0.83	0.92	0.93
Max.	[-]	1.00	0.97	0.99	1.00	1.00	1.00	0.99	0.96	1.00	0.99

Table A.6: Minimum angle

		ALL[a]	ACL	Cartilage[a]	Femur	LCL	MCL	Patella	PCL	PT	QT
<20	[#]	0	0	0	0	0	0	0	0	0	0
20-34	[#]	439	41	0	340	5	6	14	17	6	10
34-48	[#]	2662	328	6	2134	1	19	30	123	11	10
48-52	[#]	6868	338	42	6139	9	65	85	159	30	1
62-76	[#]	12041	103	198	11049	71	107	137	189	139	48
76-90	[#]	6489	0	257	5509	59	43	46	24	230	321
>90	[#]	0	0	0	0	0	0	0	0	0	0
Total	[#]	28499	810	503	25171	145	240	312	512	416	390
Min.	[°]	20.01	22.80	38.20	20.29	28.23	20.77	26.48	25.75	30.17	20.00
Average	[°]	65.41	49.60	74.66	65.53	73.19	65.51	62.86	57.36	73.61	79.44
Max.	[°]	89.17	72.00	88.46	89.17	87.57	85.82	86.00	81.09	86.26	87.63

[a]Only considering eight node solid elements.

Table A.7: Maximum angle

		ALL[a]	ACL	Cartilage[a]	Femur	LCL	MCL	Patella	PCL	PT	QT
<90	[#]	0	0	0	0	0	0	0	0	0	0
90-104	[#]	5694	1	243	4777	60	43	31	15	216	308
104-118	[#]	11486	85	200	10537	70	105	122	160	150	57
118-132	[#]	7282	308	47	6596	8	61	75	157	25	5
132-146	[#]	3077	350	11	2502	3	11	49	131	17	3
146-160	[#]	960	66	2	759	4	20	35	49	8	17
>160	[#]	0	0	0	0	0	0	0	0	0	0
Total	[#]	28499	810	503	25171	145	240	312	512	416	390
Min.	[°]	90.77	102.51	91.54	90.77	92.43	94.25	94.06	100.25	93.59	92.37
Average	[°]	116.37	132.02	106.24	116.2	107.33	115.81	122.24	126.18	106.96	101.22
Max.	[°]	159.99	159.61	159.79	159.99	157.98	159.86	159.97	159.39	157.71	158.09

[a]Only considering eight node solid elements.

A.2 Specimens

In Table A.8 anthropometrics and test details of specimens used by Ivarsson et al. [43] are tabulated.

Table A.8: Anthropometrics and details of PMHS and tests.

Test	**Weight** [kg]	**Stature**[a] [cm]	**Age** [years]	**Type**	**Direction**	**PEL** [mm]	**Length** [mm]	**LT∅** [mm]	**ST∅** [mm]	**Circ.** [mm]
1.01	72.7	193.0	51	Combined	PA	329	564	29	32	105
1.02	72.7	193.0	51	Combined	PA	330	548	30	32	102
1.03	90.9	182.9	62	Combined	PA	306	500	30	34	110
1.04	90.9	182.9	62	Combined	PA	284	491	30	34	113
1.05	81.8	177.8	62	Combined	AP	285	482	29	33	111
1.06	81.8	177.8	62	Combined	PA	285	484	28	33	105
1.07	100.0	193.0	49	Combined	PA	319	576	28	35	105
1.08	100.0	193.0	49	Combined	AP	320	572	29	34	102
1.09	100.0	185.4	62	Combined	AP	307	501	30	34	108
1.10	81.8	193.0	44	Combined	PA	306	523	27	30	102
1.11	81.8	193.0	44	Combined	PA	305	512	26	32	102
1.12	141.0	182.9	58	Combined	AP	305	518	32	35	115
1.13	141.0	182.9	58	Combined	AP	303	525	31	32	110
1.14	90.9	182.9	65	Combined	AP	304	493	26	26	99
1.15	90.9	182.9	65	Combined	PA	305	496	28	30	112
1.16	58.6	177.8	53	Combined	AP	305	492	30	30	102
1.17	58.6	177.8	53	Combined	AP	306	488	30	29	98
1.30	105.0	188.0	62	Combined	PA	292	495	34	30	101
1.34	89.0	180.3	63	Bending	AP	296	484	39	34	105
1.37	68.1	175.3	45	Bending	AP	273	441	25	27	93
1.38	68.1	175.3	45	Bending	PA	273	434	25	25	104
2.06	79.4	184.0	39	Bending	AP	277	476	29	34	105
2.07b	54.9	175.0	51	Bending	PA	286	-	26	31	108
Average:	**87.0**	**183.9**	**55**			**300**	**504**	**29**	**32**	**105**

[a]Accuracy of ± 1.3 cm
PEL-Potted External Length, LT-Lateral, ST-Sagittal, Circ.-Circumference

A.3 Load curves

In Figures A.1-A.5 all load curves obtained by the simulations of the combined loading and the three-point-bending are visualized.

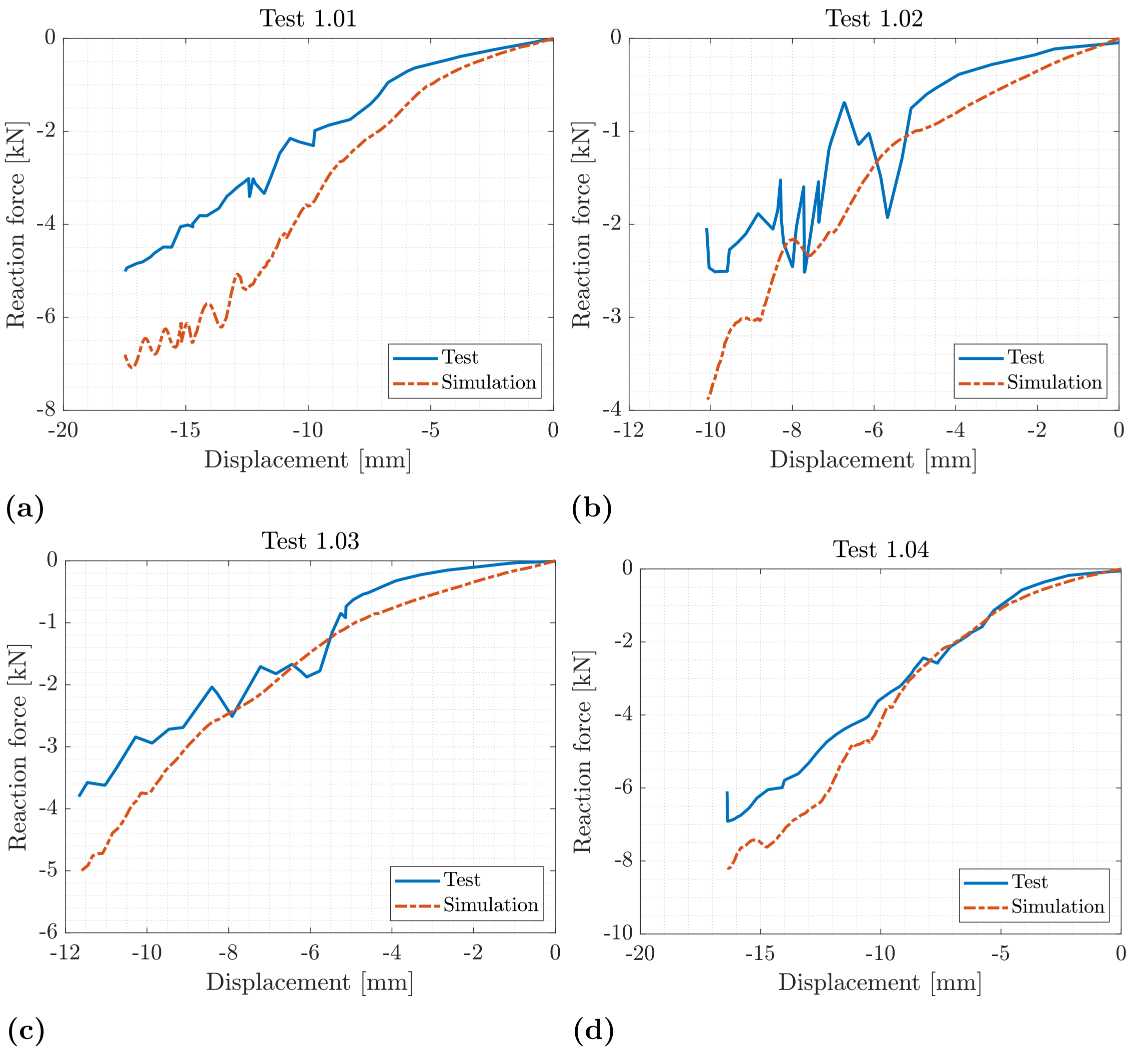

Figure A.1: Load curves for **(a)** Test 1.01, **(b)** Test 1.02, **(c)** 1.03 and **(d)** Test 1.04

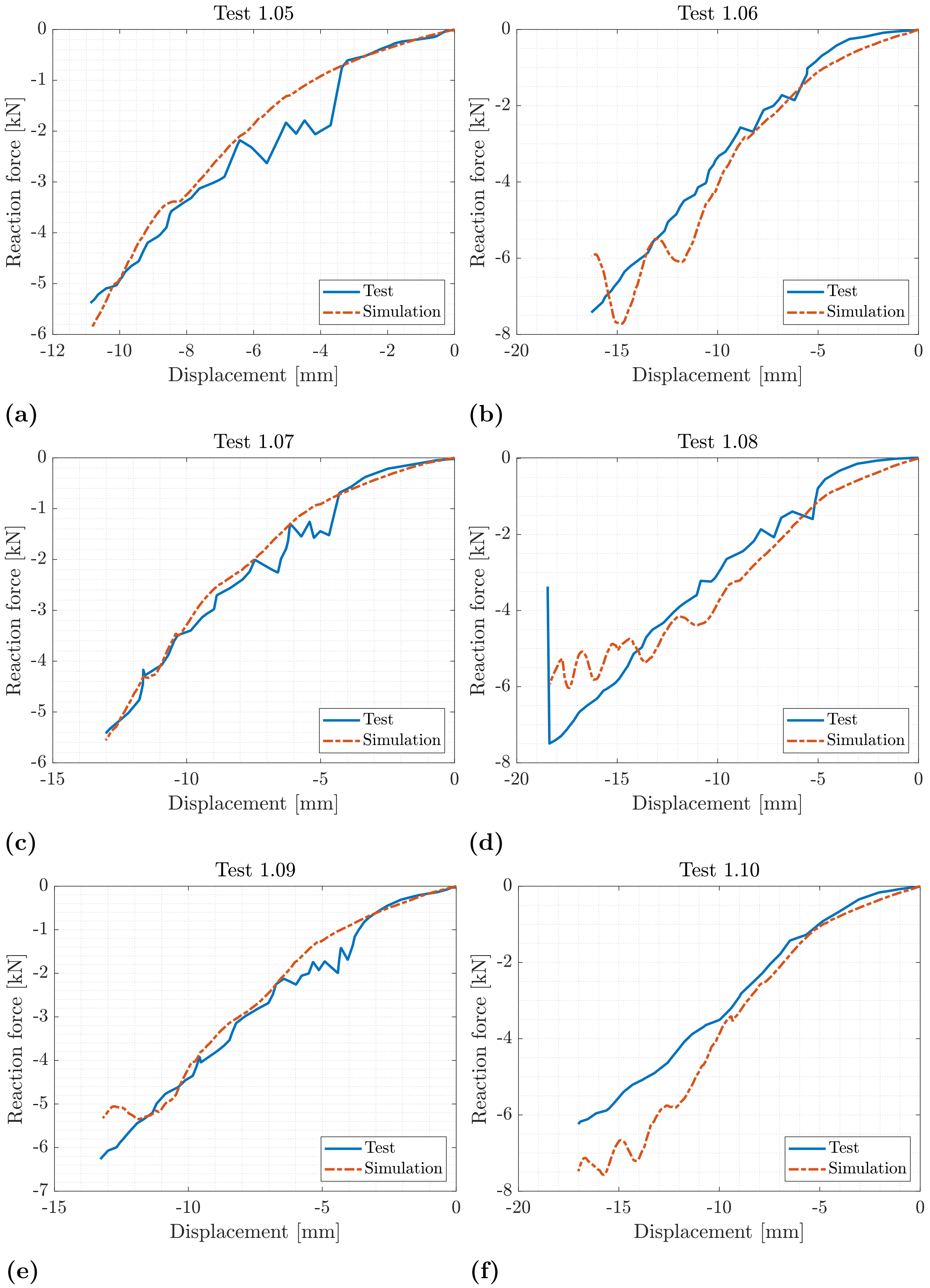

Figure A.2: Load curves for **(a)** Test 1.05, **(b)** Test 1.06, **(c)** 1.07, **(d)** Test 1.08, **(e)** Test 1.09 and **(f)** Test 1.10.

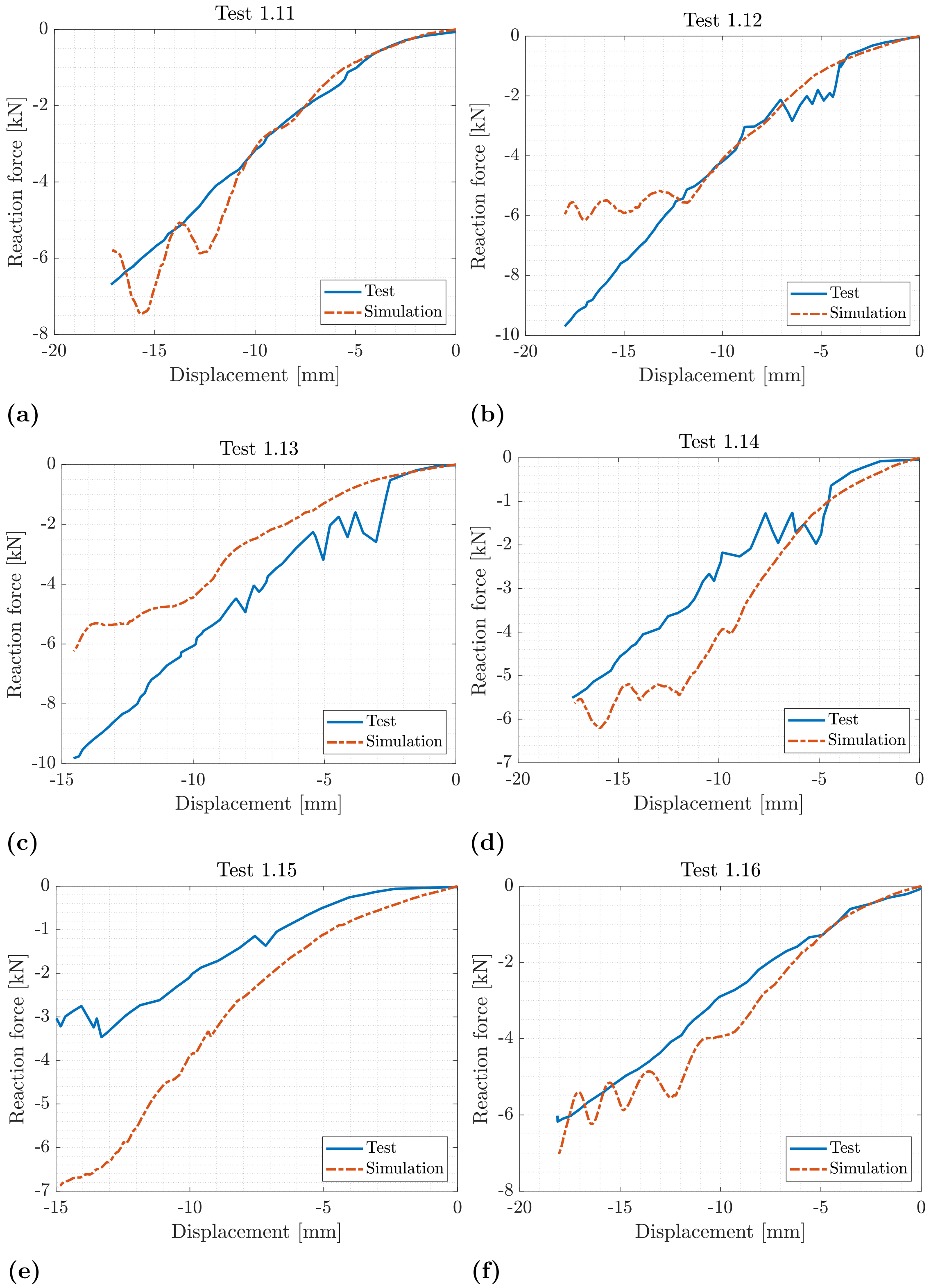

Figure A.3: Load curves for **(a)** Test 1.11, **(b)** Test 1.12, **(c)** 1.13, **(d)** Test 1.14, **(e)** Test 1.15 and **(f)** Test 1.16.

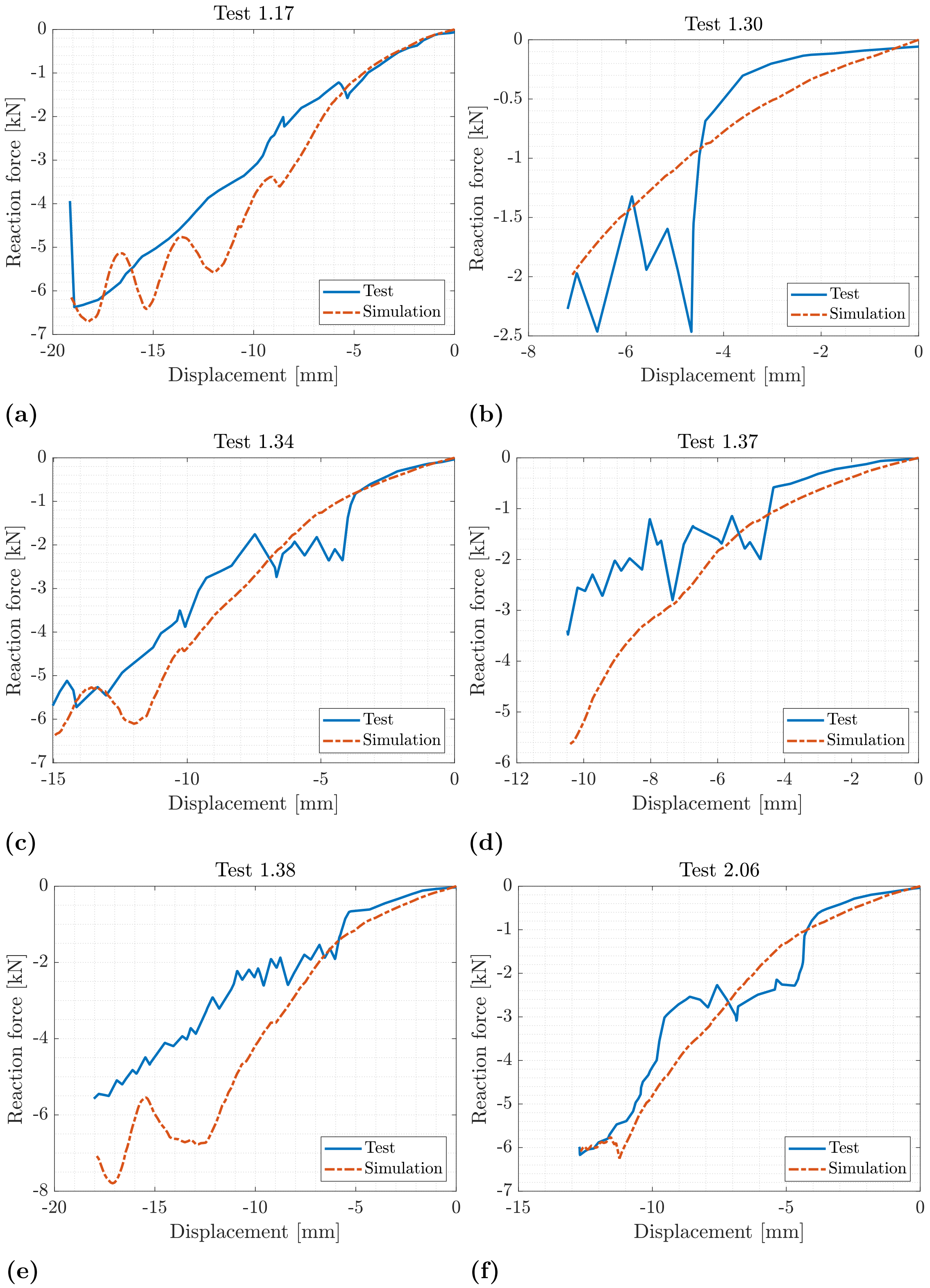

Figure A.4: Load curves for **(a)** Test 1.17, **(b)** Test 1.30, **(c)** 1.34, **(d)** Test 1.37, **(e)** Test 1.38 and **(f)** Test 2.06.

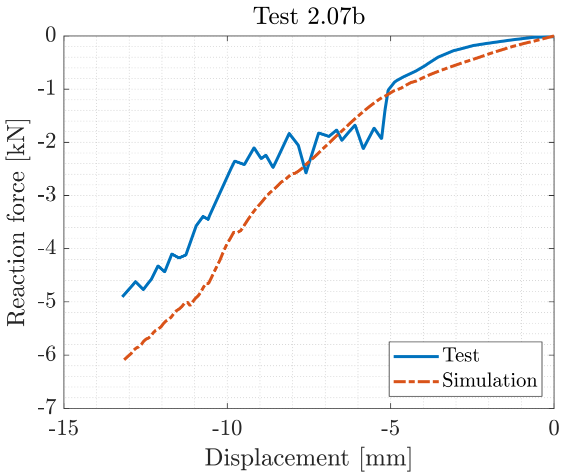

Figure A.5: Load curve for Test 2.07b.

A.4 Complete CORA evaluation

In Table A.9 the complete result of the CORA evaluation are tabulated, in Figures A.6-A.9 the time-force curves are visualized within the evaluation interval. Where the most interesting result of Table A.9 is the last column, the combined result of the two methods of the time-force comparison. Which is a metric of how well the time-force curve correlated to the time-force curve of the test.

Table A.9: Complete CORA evaluation metrics for all simulated tests.

	Test	**Cora Tot**	**Displacement**			**Force**					
			CR	**CN**	**CD**	**CR**	**CN**				**CD**
							PN	**SE**	**PE**	**Tot**[a]	
Combined loading	1.01	0.760	1.000	0.990	0.995	0.245	0.907	0.413	1.000	0.807	0.526
	1.02	0.756	1.000	0.989	0.995	0.424	0.716	0.678	0.333	0.611	0.575
	1.03	0.877	1.000	0.995	0.997	0.724	0.925	0.976	0.333	0.790	0.757
	1.04	0.897	1.000	0.997	0.999	0.678	0.993	0.656	1.000	0.911	0.794
	1.05	0.895	1.000	0.995	0.997	0.773	0.952	0.858	0.485	0.812	0.792
	1.06	0.953	1.000	0.996	0.998	0.878	0.981	0.790	1.000	0.938	0.908
	1.07	0.978	1.000	0.999	1.000	0.950	0.974	0.903	1.000	0.963	0.956
	1.08	0.912	1.000	0.995	0.998	0.833	0.963	0.671	0.678	0.818	0.826
	1.09	0.900	1.000	1.000	1.000	0.849	0.969	0.878	0.182	0.750	0.799
	1.10	0.869	1.000	0.993	0.996	0.588	0.990	0.599	1.000	0.895	0.741
	1.11	0.930	1.000	0.995	0.997	0.815	0.962	0.711	1.000	0.909	0.862
	1.12	0.881	1.000	0.998	0.999	0.741	0.950	0.531	0.712	0.786	0.763
	1.13	0.831	1.000	0.999	0.999	0.490	0.982	0.380	1.000	0.836	0.663
	1.14	0.840	1.000	0.995	0.998	0.578	0.959	0.698	0.523	0.785	0.681
	1.15	0.757	1.000	0.991	0.995	0.231	0.990	0.242	1.000	0.805	0.518
	1.16	0.973	1.000	0.995	0.998	0.936	0.979	0.891	1.000	0.962	0.949
	1.17	0.928	1.000	0.996	0.998	0.837	0.948	0.967	0.658	0.881	0.859
	1.30	0.780	1.000	0.994	0.997	0.645	0.685	0.542	0.000	0.478	0.562
	Average:	**0.873**	**1.000**	**0.995**	**0.998**	**0.679**	**0.935**	**0.688**	**0.717**	**0.819**	**0.752**
3pt bending	1.34	0.918	1.000	0.993	0.997	0.766	0.918	0.756	1.000	0.913	0.840
	1.37	0.767	1.000	0.996	0.998	0.487	0.891	0.379	0.182	0.586	0.536
	1.38	0.807	1.000	0.996	0.998	0.482	0.933	0.561	0.612	0.752	0.617
	2.06	0.914	1.000	0.974	0.987	0.831	0.917	0.953	0.612	0.850	0.840
	2.07b	0.879	1.000	0.978	0.989	0.660	0.930	0.652	1.000	0.878	0.769
	Average:	**0.857**	**1.000**	**0.987**	**0.994**	**0.645**	**0.918**	**0.660**	**0.681**	**0.796**	**0.720**

[a] Weighted factor of PN, SE and PE.
CR- Corridor, CN- Cross-Correlation, CD- Combination of CR and CN, PN- Progression, SE- Size and PE- Phase.

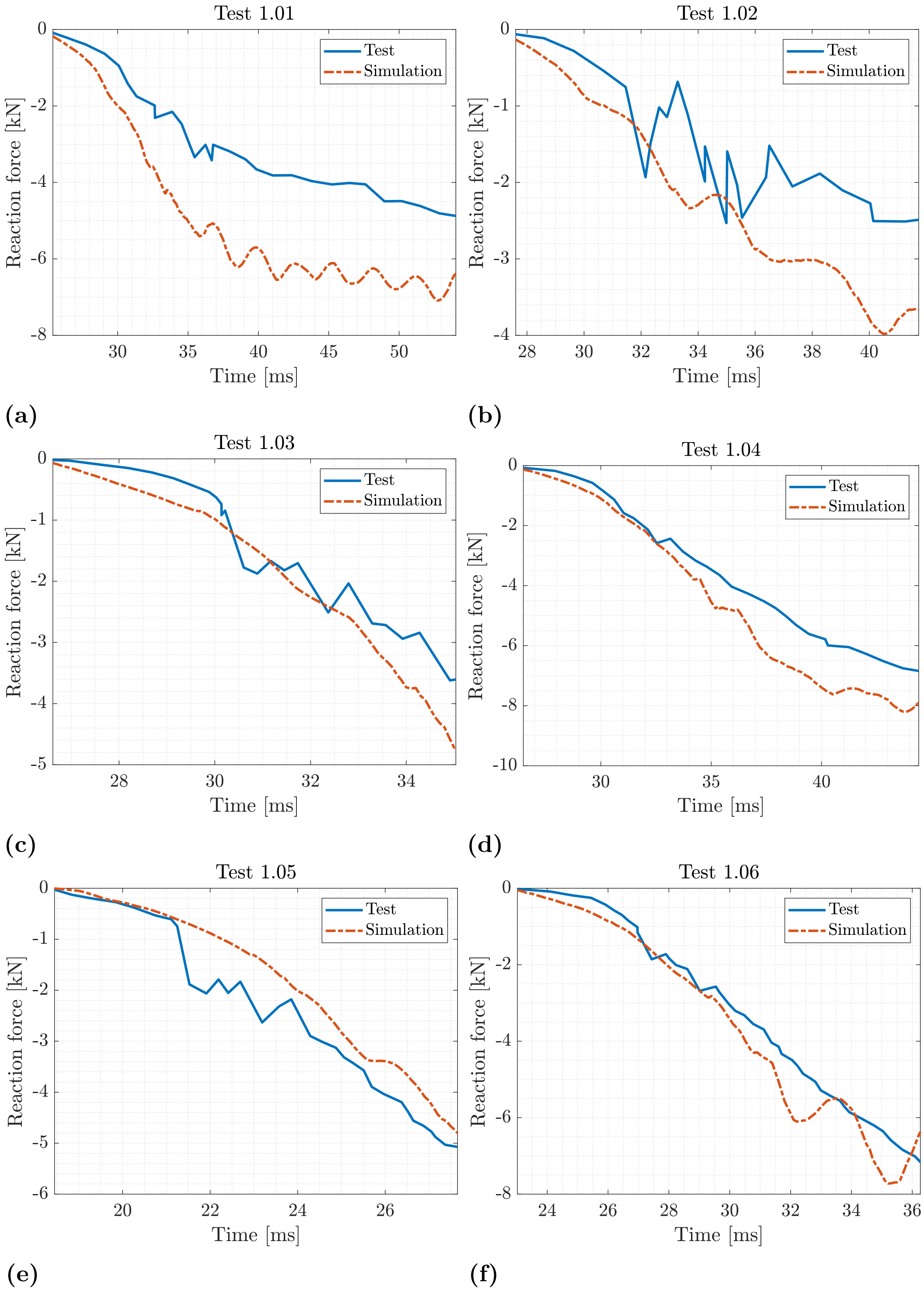

Figure A.6: Time-force curves for **(a)** Test 1.01, **(b)** Test 1.02, **(c)** 1.03, **(d)** Test 1.04, **(e)** Test 1.05 and **(f)** Test 1.06.

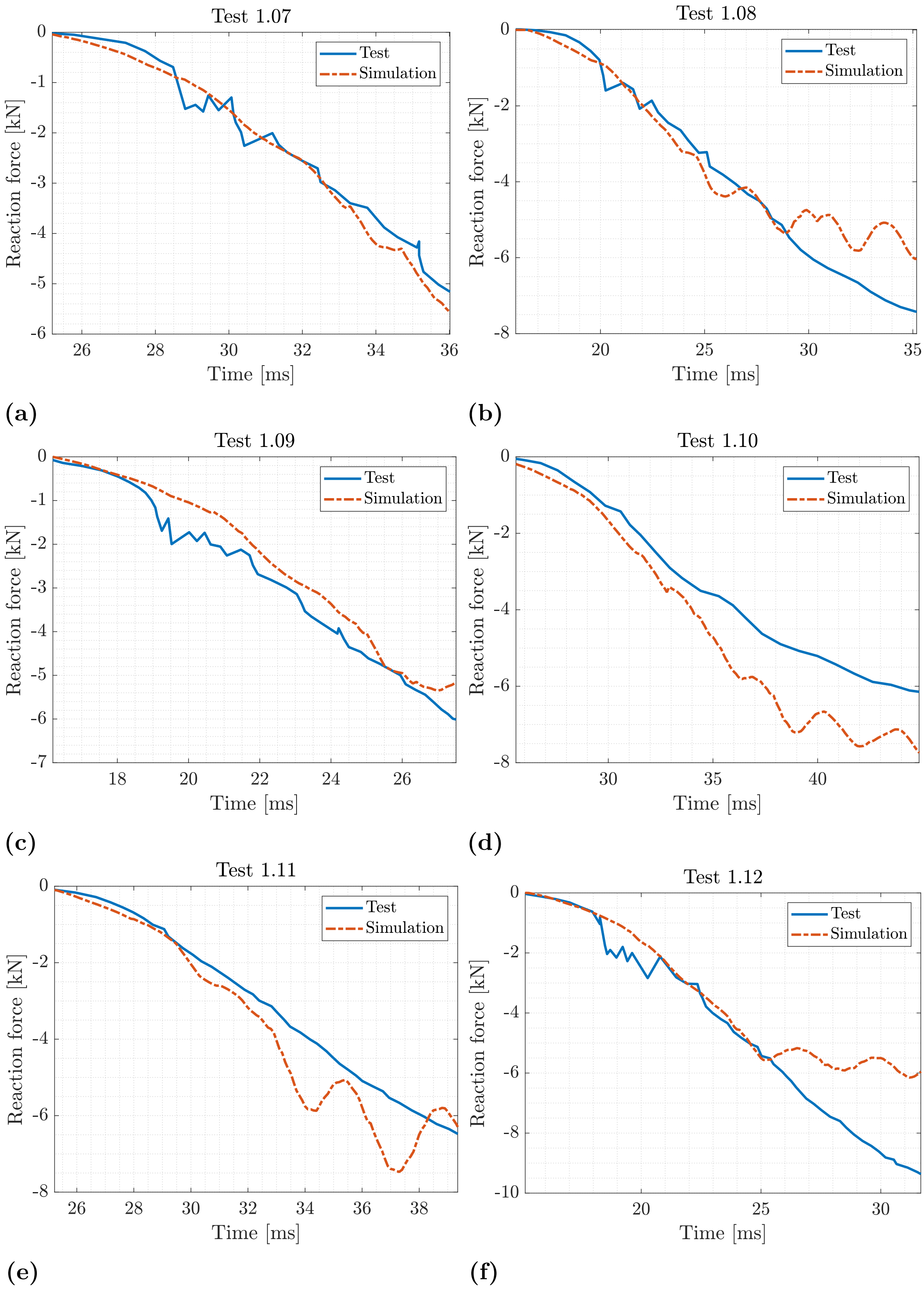

Figure A.7: Time-force curves for **(a)** Test 1.07, **(b)** Test 1.08, **(c)** 1.09, **(d)** Test 1.10, **(e)** Test 1.11 and **(f)** Test 1.12.

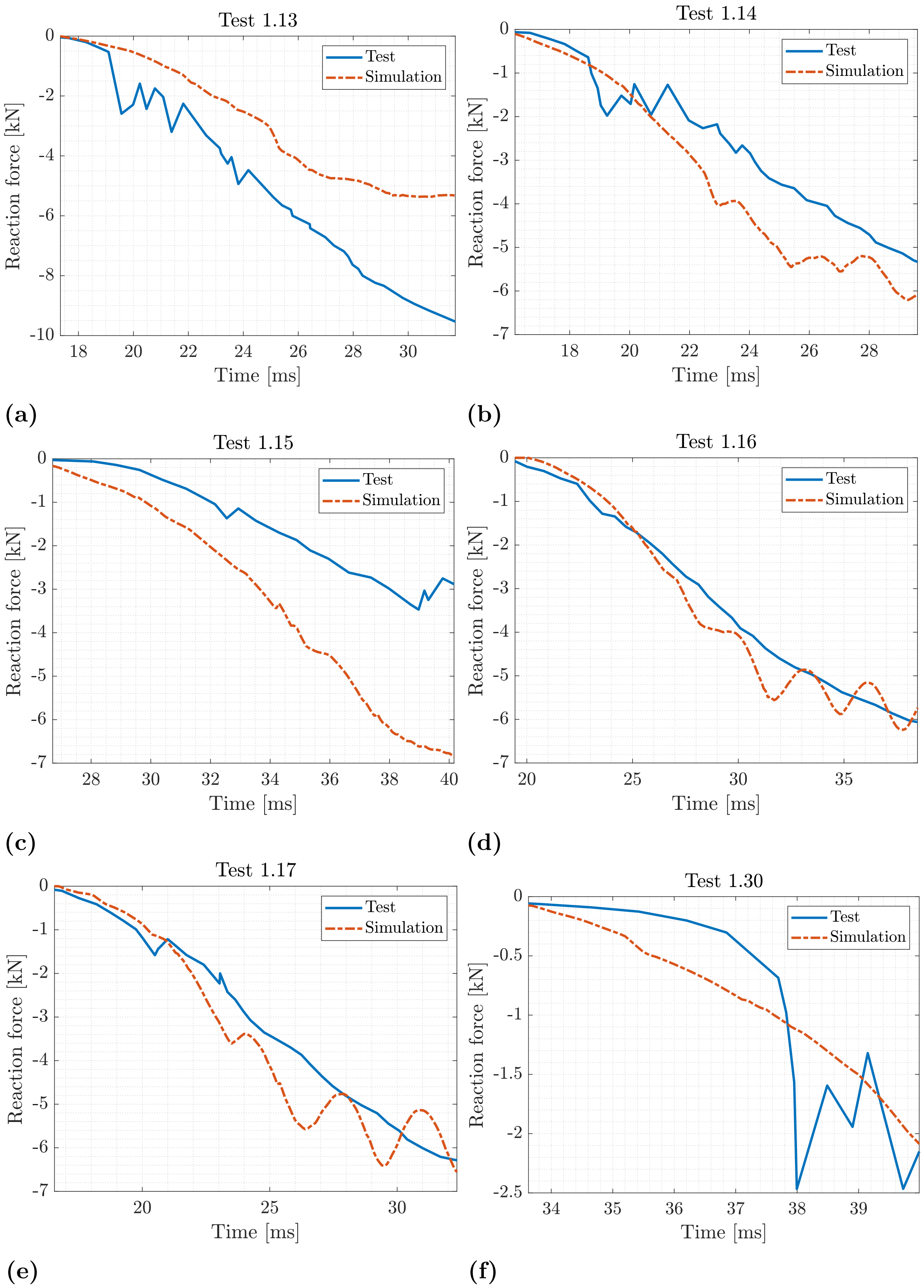

Figure A.8: Time-force curves for **(a)** Test 1.13, **(b)** Test 1.14, **(c)** 1.15, **(d)** Test 1.16, **(e)** Test 1.17 and **(f)** Test 1.30.

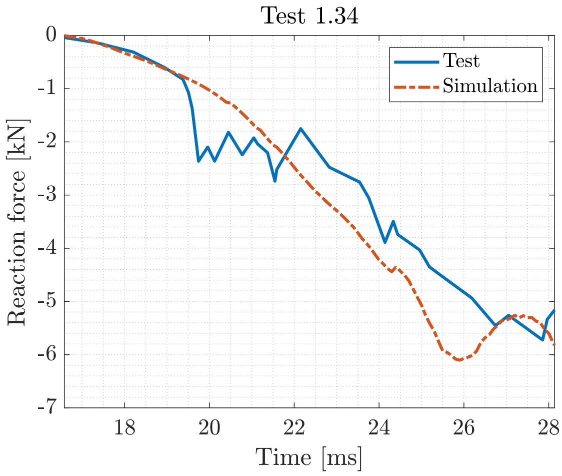

(a)

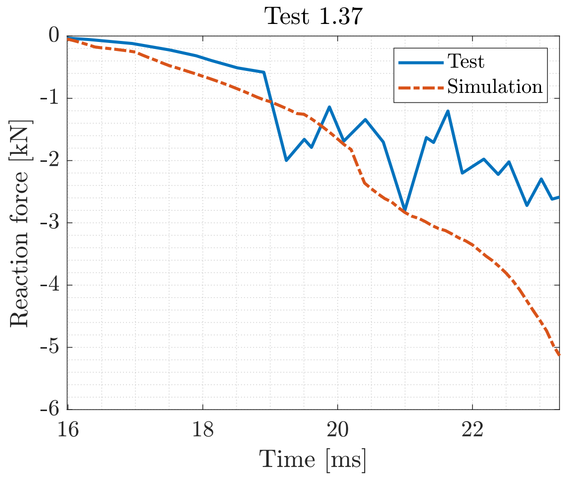

(b)

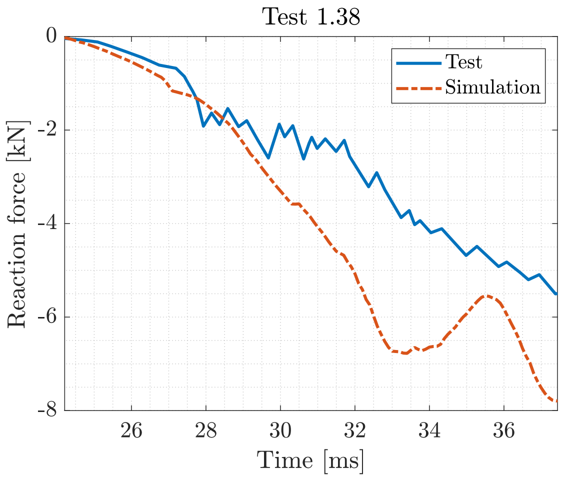

(c)

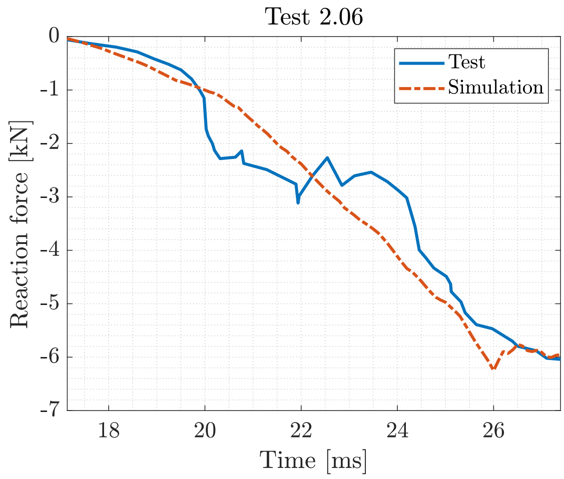

(d)

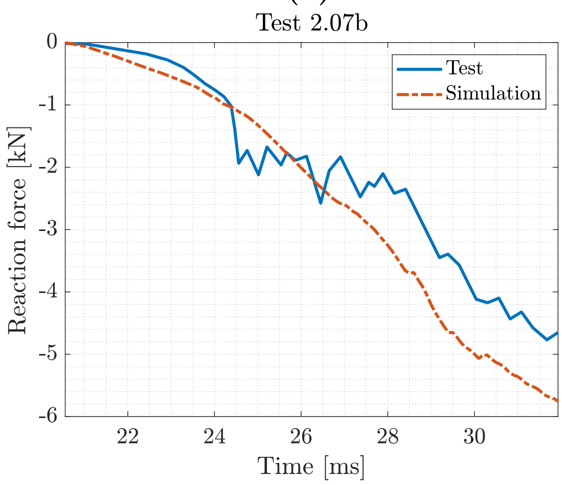

(e)

Figure A.9: Time-force curves for **(a)** Test 1.34, **(b)** Test 1.37, **(c)** 1.38, **(d)** Test 2.06 and **(e)** Test 2.07b.

DEPARTMENT OF MECHANICS AND MARITIME SCIENCES
CHALMERS UNIVERSITY OF TECHNOLOGY
Gothenburg, Sweden 2022
www.chalmers.se

AVANCEZ
1829

CHALMERS
UNIVERSITY OF TECHNOLOGY